Science & Technology Facilities Council

Technical Report
RAL-TR-2015-014
(corrected)

SCARF Annual Report 2014-2015

D Ross (ed)

December 2015 (corrected December 2015)

Enquiries concerning this report should be addressed to:

RAL Library
STFC Rutherford Appleton Laboratory
Harwell Oxford
Didcot
OX11 0QX

Tel: +44(0)1235 445384
Fax: +44(0)1235 446403
email: libraryral@stfc.ac.uk

Science and Technology Facilities Council reports are available online at: http://epubs.stfc.ac.uk

ISSN 1358-6254

Science & Technology Facilities Council

SCARF Annual Report 2014-2015

Version: 1.0

Date: 23/11/2015

Edited by Derek Ross (derek.ross@stfc.ac.uk) 01235 445651

Content written by the respective authors

Date	Revision	Changes
13/10/15	0.1	Initial document
26/10/15	0.2	Add more science contributions
20/11/15	0.3	Add presentation and publications Update all non-science contribution sections
23/11/15	1.0	First release

Abstract

Annual Report on the Usage and Scientific Impact of the SCARF Service

Dissemination

This is a public document

1 SCARF SERVICE

SCARF is a High Performance Cluster for STFC staff, Facilities (ISIS, DIAMOND, CLF) and their users. The SCARF Service was started in 2004 and has been upgraded year on year and now represents a significant capital investment in High Performance Computing. Overall SCARF now has over 5400 CPU cores, 25TB memory and 160TB of disk space (Details in Appendix 1).

This report covers the year 2014-15 and outlines the research that SCARF has enabled.

1.1 SCARF Usage by Department

Each time a researcher uses the SCARF service the CPU time used is recorded. In total over 500,000 jobs, using 26M CPU hours, were submitted to SCARF during 2014-15.

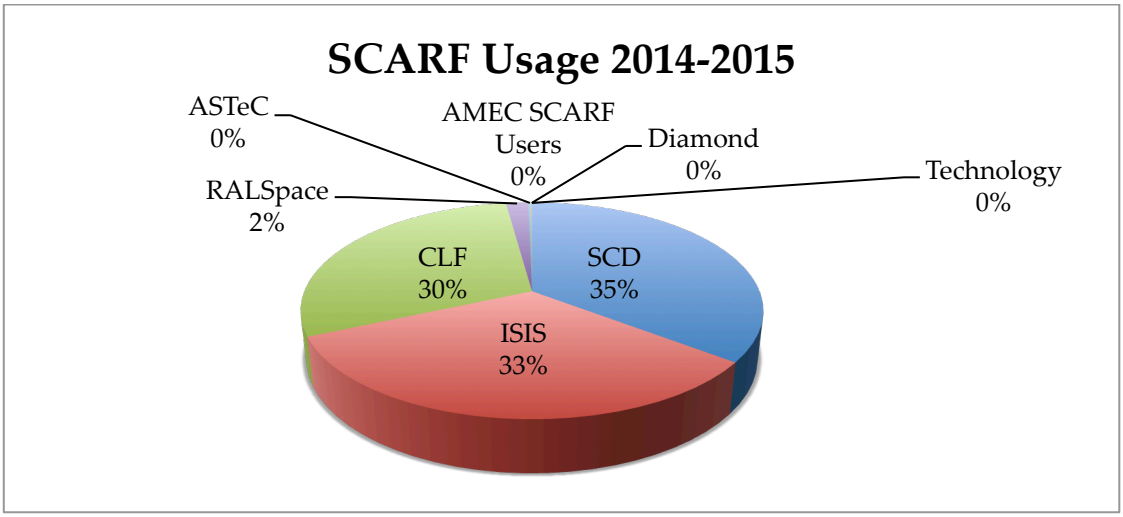

Figure 1.1.1: Pie chart showing percentage usage of the SCARF service by department

It is clear from the usage chart that ISIS, CLF and Scientific Computing are the largest users of SCARF. The table below breaks down the usage further, showing usage from users collaborating with STFC departments and other external groups that have access to SCARF including groups from the University of Strathclyde, Amec Foster Wheeler and the University of Parma.

	2014-15			2013-14			2012-13		
Dept	**Active Users**	**CPU hrs**	**%**	**Active Users**	**CPU hrs**	**%**	**Active Users**	**CPU hrs**	**%**
SCD	49	8210127.49	31.4	37	8980895.60	47.1	27	3432184.71	41.0
ISIS	25	4944363.74	18.9	23	2858306.49	15.0	17	2200465.95	26.3
External	37	6716465.17	25.7	22	4748211.01	24.9	23	1697806.08	20.3
CLF	19	5298080.49	20.3	29	2010153.36	10.5	23	1099791.25	13.1
ISIS_IBIS	6	43465.14	0.17	6	68371.04	0.36	5	107783.83	1.3
DIAMOND	6	141874.42	0.54	3	5970.4	0.0	0	0.0	0.0
ASTEC	3	45641.77	0.17	3	112843.12	0.6	7	48549.59	0.6
RAL Space	4	718069.17	2.8	2	267668.469	1.4	2	215804.818	2.6
Totals	**149**	**26118087**	**100**	**128**	**19055284**	**100**	**100**	**8375330.95**	**100**

Figure 1.1.2: Table displaying detailed usage from 2014-15 comparing with 2013-14 and 2012-13

A significant amount of computational resource has been used on SCARF; section 3 highlights some of the scientific achievements that have been enabled.

1.2 SCARF Availability

The aim is to keep SCARF available to users as much as possible, this year there were a number of interventions to migrate hardware to a new network topology, but no planned interventions that required the entire cluster to be shutdown. There were a number of network breaks and an issue with the backend storage system that caused unplanned interventions.

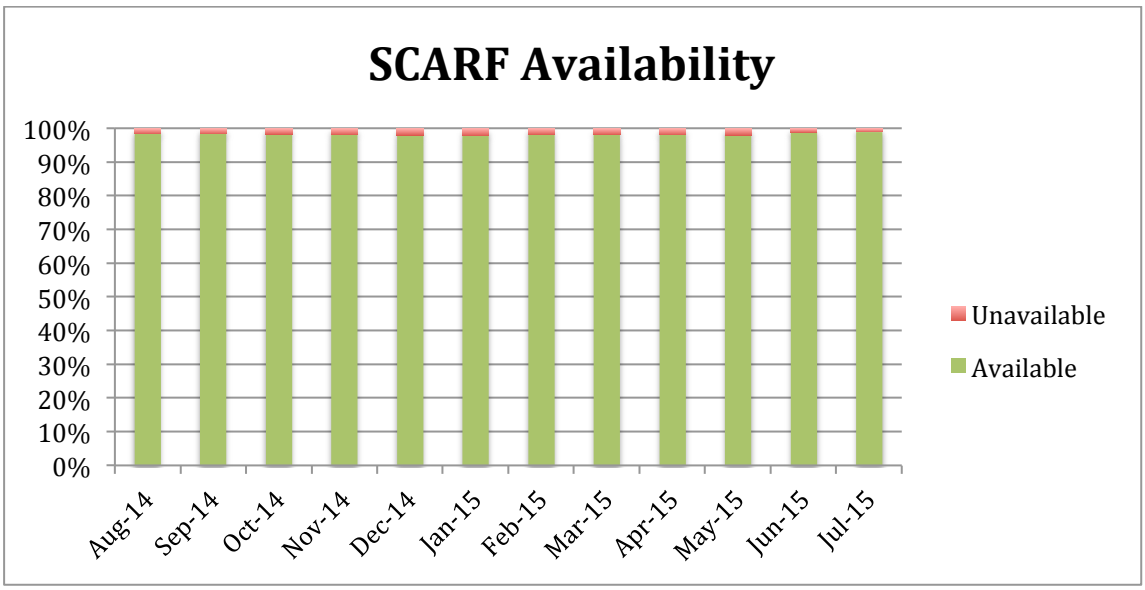

Figure 1.2.1: Availability for SCARF

As can can be seen in the table below, the oldest hardware is the least available, supporting the yearly refresh cycle.

Year Purchased	Compute node Availability 2014-15	Compute node Availability 2013-14	Compute node Availability 2012-13
2010	96.56%	99.99%	99.1
2011	100.00%	99.88%	98.9
2012	100.00%	99.95%	98.9
2013	99.33%	99.80%	100%
2014	100.00%	100.00%	N/A
2015	99.99%	N/A	N/A

Figure 1.2.2: Availability vs. Year Purchased

1.3 SCARF Developments 2014-15

Major SCARF Developments are listed below. A more detailed list can be found in Appendix 5

- New capacity added
  - 1360 Intel E5-2650v3 CPU cores for general use went into production in June 2015

1.4 Future Development

SCARF 2016 Hardware Upgrade

- Storage Upgrade
- Compute upgrade

Migration to RHEL7

1.5 Help and Support

For any queries concerning the SCARF service please email the SCARF Helpdesk

scarf@hpc-support.rl.ac.uk

2 PUBLICATIONS AND PRESENTATIONS

2.1 Publications

A list of publications is give is Appendix 3. A way of estimating the impact that SCARF has had is to analyse the Journal Impact Factor using the Journal Citation Reports published by Thomson Reuters (2014). The average Impact Factor for Journals published as a result of using SCARF is 4.00. This compares to a median impact factor across all 8659 journals of 1.451. This is a simplistic analysis but demonstrates that the science done on SCARF is having an impact.

2.2 Presentations

Scientists have presented their work at 11 international conferences (Appendix 3). This helps to demonstrate that the science enabled by SCARF is world class.

3 SCIENCE HIGHLIGHTS

3.1 Characterisation of C_{70} by vibrational spectroscopy and periodic density functional theory

Keith Refson,[a,b] and Stewart F. Parker *[a]

[a]ISIS Facility, STFC Rutherford Appleton Laboratory, Chilton, Didcot, OX11 0QX, UK
[b]Department of Physics, Royal Holloway, University of London, Egham TW20 0EX, UK

The fullerene C_{70}, Fig. 3.1.1, may be considered as the shortest possible nanotube capped by a hemisphere of C_{60} at each end. Vibrational spectroscopy is a key tool in characterising fullerenes [1] and C_{70} has been studied several times and spectral assignments proposed. Unfortunately, many of the modes are either forbidden or have very low infrared or Raman intensity, even if allowed. Inelastic neutron scattering (INS) spectroscopy is not subject to selection rules and all the modes are allowed. We have obtained a new INS spectrum from a large sample recorded at the highest resolution available. An advantage of INS spectroscopy is that it is straightforward to calculate the spectral intensity from a model. We have used periodic density functional theory as implemented in CASTEP [2] on SCARF to carry out a geometry optimisation of C_{70} in one of the proposed low-temperature structures and then calculated the INS, infrared and Raman spectra. The calculated geometry is in good agreement with the experimental data and Figs. 3.1.1, 3.1.2 compare the observed and calculated INS, infrared and Raman spectra [3].

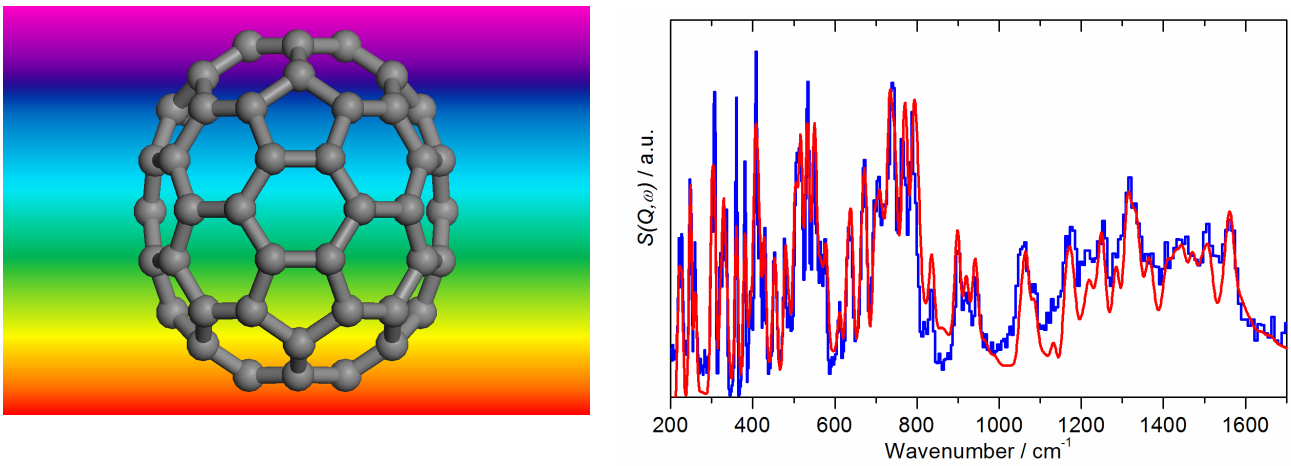

Figure 3.1.1: Left: the structure of C_{70}. Right: Comparison of the TOSCA INS spectrum of C_{70} at 7 K (blue) with that calculated for the solid state by CASTEP (site symmetry C_s) after individual scaling of the modes and inclusion of the phonon wings.

It can be seen that the agreement for the INS and Raman spectra is excellent and demonstrates what is achievable with state-of-the-art computational resources. The observed infrared spectrum has many more features than the calculation predicts. However, there is good agreement with the vibrational density of states (VDOS). It is not at all clear why this occurs. The infrared spectrum was recorded by attenuated total internal reflection (ATR) and the device uses a clamp to ensure good contact between the sample and the diamond ATR element. However, pressure alone cannot be the explanation as transmission infrared measurements[4] up to 10 GPa do not result in a similar spectrum. We (and others [5]) have observed a similar effect in C_{60}.

A combination of a much better quality INS spectrum with periodic DFT calculations has allowed all the internal modes of C_{70} to be assigned. Comparison of the INS spectra predicted by previous work with the new data demonstrates that all previous assignments were incorrect in several respects. In particular, isolated molecule calculations using Gaussian basis sets result in inaccurate assignments. In contrast, the periodic-DFT approach produces assignments that are in almost quantitative agreement with the data without the need for scaling for both C_{60} and C_{70}. This clearly has implications for the future assignment of higher fullerenes such as C_{84}.

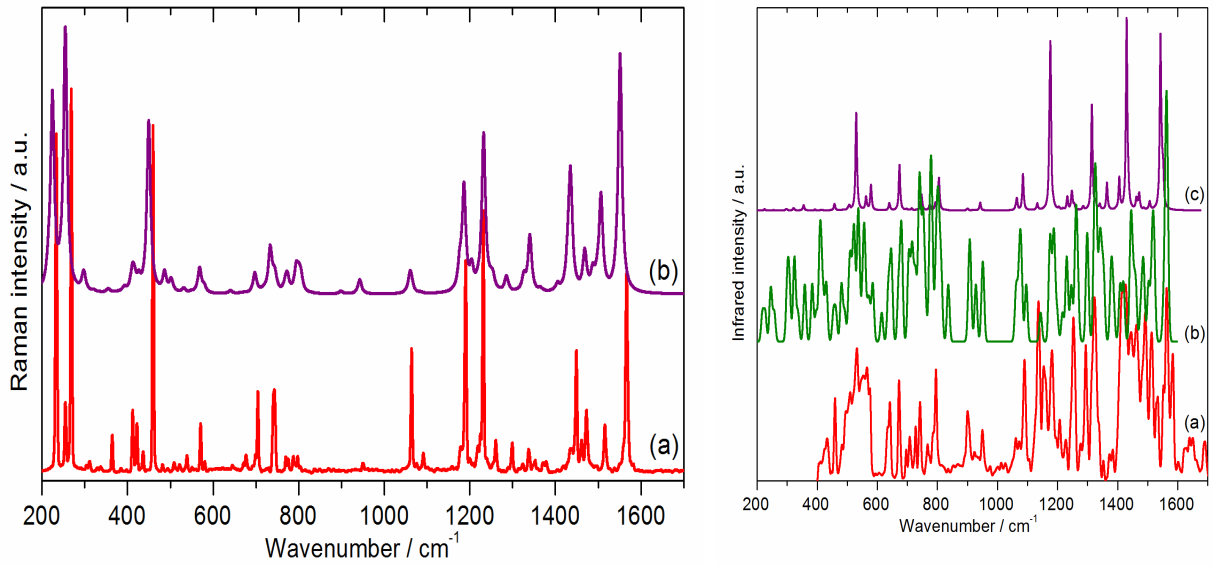

Figure 3.1.2: Left: comparison of: (a) the observed Raman spectrum of C70 at 7 K with (b) that calculated for the solid state. Right: Comparison of: (a) the observed infrared spectrum of C70 at 113 K with (b) the calculated VDOS and (c) calculated infrared spectrum. All calculated spectra are for the solid state by CASTEP with Cs site symmetry.

References

[1] S. F. Parker, S. M. Bennington, J. W. Taylor, H. Herman, I. Silverwood, P. Albers. K. Refson, *Phys. Chem. Chem. Phys.* **2011**, 13, 7789.

[2] S. J. Clark, M. D. Segall, C. J. Pickard, P. J. Hasnip, M. J. Probert, K. Refson, M. C. Payne, *Z. Krist.* **2005**, *220*, 567.

[3] K. Refson and S.F. Parker, *ChemistryOpen*, (2015) [doi: 10.1002/open.201500069].

[4] K. Thirunavukkuarasu, V. C. Long, J. L. Musfeldt, F. Borondics, G. Klupp, K. Kamarás, C. A. Kuntscher, *J. Phys. Chem. C* **2011**, *115*, 3646.

[5] A. Rassat, C. Fabre, A. Messaoudi, R. Setton, R. Ceolin, P. Bernier, A. Zahab, *Compt. Rendus Acad. Sci. Paris, Série 2*, **1992**, *315*, 1653.

3.2 Simulating of the Lunar swirls leading the way to protect spacecraft from cosmic rays.

Ruth Bamford, RAL Space and CLF, Raoul Trines and Bob Bingham, CLF

On the near side of the Moon, located on one of the dark, most ancient plateaus of the Moon, there is an unusual white swirl marking that appears to bear no relation to any typical impact craters or lunar ejecta. Visible from Earth, the Reiner Gamma Formation is the quintessential example of a lunar swirl.

The lunar surface darkens with age due to space weathering from the bombardment of solar wind protons. The presence of small, 10-1000km, regions of unweathered lunar surface where no topographical cause can be determined, have been an intriguing astronomical phenomena for centuries.

During the early Apollo missions it was discovered that the location and size of lunar swirls coincide with small (~100s~km) surface patches of crustal magnetic field. The Moon is without either an atmosphere or an overarching magnetic field, unlike the Earth's, that would erode and disperse differences in rates of space weathering maturation. The lunar swirl markings therefore represent a time integrated record of the ability of low intensity magnetic fields (~1/100th) that at the Earth's surface) to shield parts of the Moon's surface from proton bombardment. The fine detail visible within the swirls points to a very precise and consistent control of the proton flux. Understanding how this works could lead to the ability to artificially recreate and enhance the protective effects for people and instrumentation susceptible to damage from the more intense parts of the cosmic radiation.

In the paper titled, *Simulated signatures from mini-magnetospheres and comparison with Lunar observational data and theory*, by Bamford et. al., the use of 2D and 3D particle-in-cell plasma simulations run in part on SCARF system, are used to show how finite Larmor orbit plasma effects reproduce the small scale deflection, reflection and retardation of incoming interplanetary plasma with the detail level of the lunar swirls and the plasma observations recorded by surveying spacecraft.

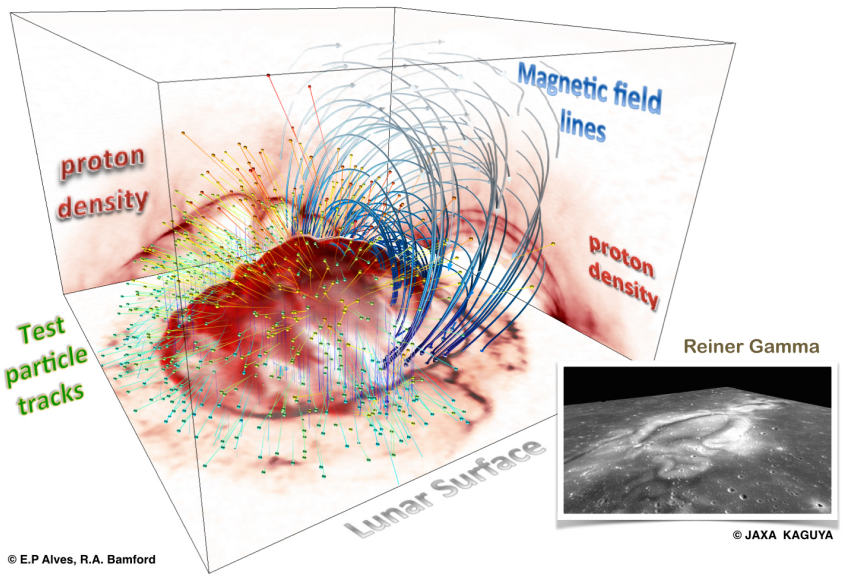

Figure 3.2.1: OSIRIS 3-D plasma particle-in-cell code simulation of a Lunar crustal magnetic anomaly shielding the parts of the surface of the Moon and believed to be responsible for the formation of white discolourations on the surface known as 'Lunar Swirls. The archetype example of which is Reiner Gamma

– a photograph of which is shown in the insert. The inclined angle photograph was taken by the Japanese Space Agency, JAXA, spacecraft KAGUYA, at low altitude ~100km altitude. The central region of Reiner Gamma is about 100km across . The unusual lunar albedo 'swirl' is co-incident with an anomalised patch of crustal magnetic field of about 300nT at the surface shown in the low altitude photograph

References

Bamford, R., "*Simulated signatures from mini-magnetospheres and comparison with Lunar observational data and theory*", Paper Submitted to The Astronomical Journal, 2015.

Bamford, R. A., et al. "*Formation of Lunar Swirls*." *arXiv preprint arXiv:1505.06304* (2015).

3.3 Implications for Manned Spacecraft

Ruth Bamford, RAL Space and CLF, Raoul Trines and Bob Bingham, CLF

If mankind is to explore the solar system beyond the confines of our Earth and Moon the problem of radiation protection must be addressed. Galactic cosmic rays and highly variable energetic solar particles are an ever-present hazard in interplanetary space.

Electric and/or magnetic fields have been suggested as deflection shields in the past, but these treated space as an empty vacuum. In fact it is not empty. Space contains a plasma known as the solar wind; a constant flow of protons and electrons coming from the Sun.

In the paper titled *An exploration of the effectiveness of artificial mini-magnetospheres as a potential solar storm shelter for long term human space missions* by Bamford et al., we explore the effectiveness of a "mini-magnetosphere" acting as a radiation protection shield. We explicitly include the plasma physics necessary to account for the solar wind and its induced effects. We show that, by capturing/containing this plasma, we enhance the effectiveness of the shield. Further evidence to support our conclusions can be obtained from studying naturally occurring "mini-magnetospheres" on the Moon. These magnetic anomalies (related to "lunar swirls) exhibit many of the effects seen in laboratory experiments and computer simulations. If shown to be feasible, this technology could become the gateway to manned exploration of interplanetary space.

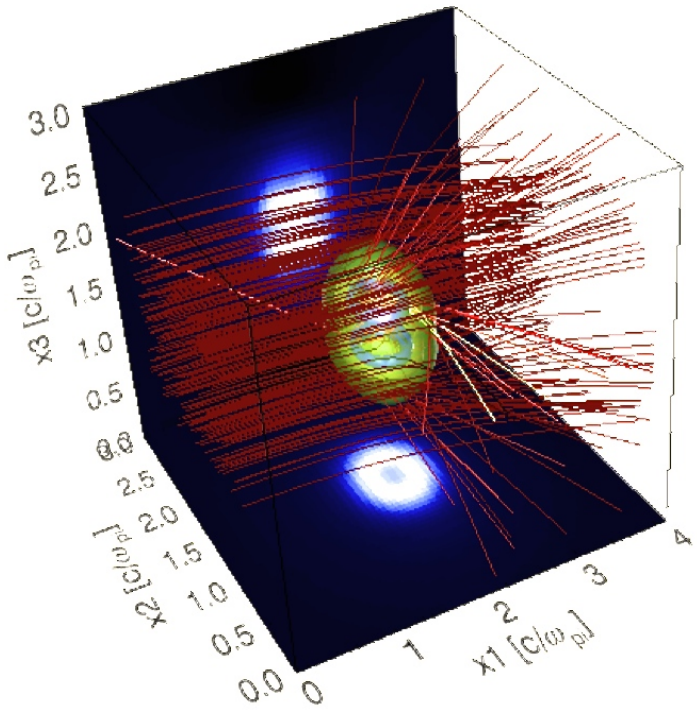

Figure 3.3.1: A simulation of particle tracks (red) scattered from a thin electrostatic "shell" (green) surrounding a magnetic dipole (cente with B field intensity projected onto the faces of the cube). The particles are not being deflected by the magnetic field but by the electric field resulting from the interaction of the background plasma (omitted for clarity) and the magnetic field. The energy of the red 'protons' is 100,00 times that of the background plasma. Simulation is in dimensionless units.

References

Bamford, R. A., et al. "*An exploration of the effectiveness of artificial mini-magnetospheres as a potential solar storm shelter for long term human space missions*." *Acta Astronautica* 105.2 Dec (2014): 385-394

3.4 Summary of ConnectFlow Activities on SCARF 2015

Steve Joyce, Amec Foster Wheeler

Amec Foster Wheeler has developed a facility in their ConnectFlow groundwater modelling software to couple calculations of groundwater flow, solute transport and chemical reactions (Joyce et al. 2014a). When carried out on a large scale, these calculations are very computationally demanding. Therefore, to make these calculations practicable it is necessary to have an efficient implementation that takes full advantage of modern multi-processor technologies.

The most demanding parts of the simulations in terms of performance are the calculations of chemical reactions. Fortunately, many of these calculations can be carried out independently and so lend themselves readily to parallelisation. Likewise, the transport of each chemical species can be calculated separately and hence parallelised (up to the point where there is one species per process). The calculations were parallelised in ConnectFlow using MPI and the scalability was tested on the STFC SCARF cluster at the Rutherford Appleton Laboratories.

Figure 3.4.1 shows how the simulation performance scales with the number of CPU cores for different parts of the calculation. It can be seen that the calculation time drops very rapidly as more cores are added. The performance scaling relative to a single core is also good up to the 128 cores tried. As expected, the scaling of the transport calculations flattens off once there are more cores than species to transport. It is intended that further improvements can be made to improve the scalability further, particularly on multiple nodes where data handling efficiencies are important.

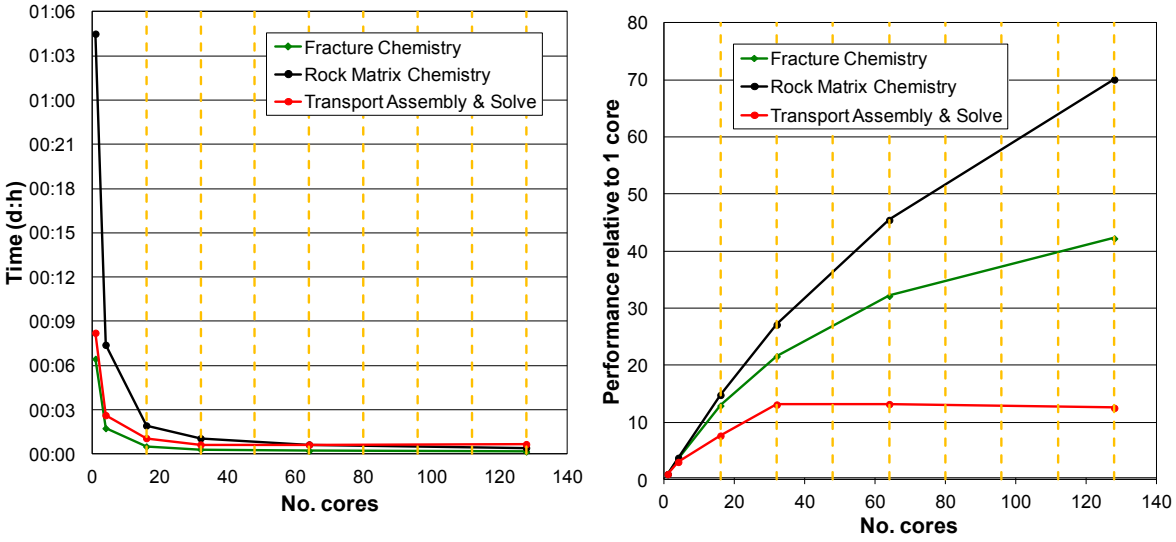

Figure 3.4.1: Scaling of ConnectFlow reactive transport performance with number of CPU cores. Vertical dashed lines indicate when an additional SCARF node is used.

This ConnectFlow functionality has been successfully applied to a regional-scale model of a proposed geological spent nuclear fuel repository at Forsmark in Sweden on behalf of the Swedish Nuclear Fuel and Waste Management Company (SKB). The simulations calculated the evolution of groundwater composition around the repository over a 68,000 year temperate climate period. Figure 3.4.2 shows how the chloride mass fraction changes between 2,000 AD and 60,000 AD due the infiltration of dilute meteoric water. The work was presented in September at the Migration

2015 conference in Santa Fe (Joyce et al. 2015) and has also been published in an SKB report (Joyce et al. 2014b). There are plans to produce a journal paper on this work later in the year.

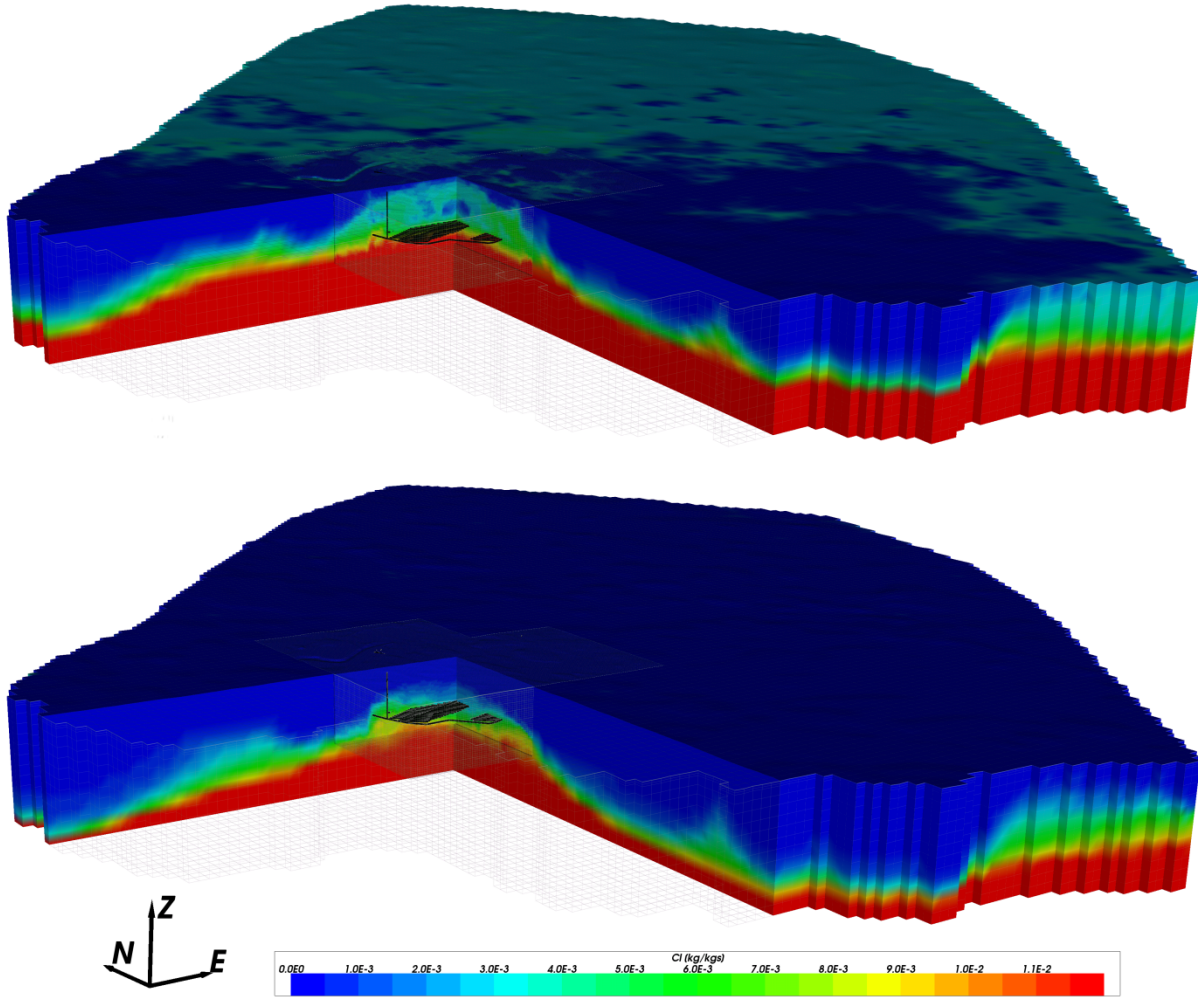

Figure 3.4.2: Chloride mass fractions in a regional scale model of Forsmark at 2,000 AD (top) and 60,000 AD (bottom). Part of the model has been cut away and the repository layout added (in black) for illustration.

References

[1] Joyce S, Applegate D, Appleyard P, Gordon A, Heath T, Hunter F, Hoek J, Jackson P, Swan D, Woollard H, 2014a. Groundwater flow and reactive transport modelling in ConnectFlow. SKB R-14-19, Svensk Kärnbränslehantering AB.

[2] Joyce S, Woollard H, Marsic N, Sidborn M, 2014b. Future evolution of groundwater composition at Forsmark during an extended temperate period. SKB R-14-26, Svensk Kärnbränslehantering AB.

[3] Joyce S, Hartley L, Woollard H, Marsic N, Sidborn M, Gylling B, Puigdomenech I, Koskinen L, 2015. Coupled groundwater flow and reactive transport regional-scale simulations of the evolution of groundwater chemistry for a geological spent nuclear fuel repository. Oral presentation at the Migration 2015 conference, Sante Fe, New Mexico, USA.

3.5 Ab initio investigations of the excited states of organic molecular probes of clay minerals using CASTEP[1]

Dawn Geatches, STFC Daresbury Laboratory

Clay minerals are layered aluminosilicate minerals widely formed by the weathering and decomposition of rocks. Their layered structure endows them with proportionally larger surface area to volume ratios, varying particle thickness, as well as all of the potential 'defects', kinks and variety of edges expected within any analogous manmade nano-particle. Further complexity is added by the layers being negatively charged, which attracts positive counter-ions to sorb between the layers with a wide variety of ions producing both the positive and negative charges. Consequently, the difficult task of characterising the structure, charge density and charge location of the clay minerals is often achieved from the excited state spectra of a molecular probe such as the cationic dye methylene blue (MB^+ – monomer; MB^{2+} - dimer), which readily sorbs to clay mineral surfaces.

The work undertaken on SCARF involved testing the time dependent density functional theory (TDDFT) module of CASTEP on a kaolinite/MB^+/MB^{2+} model system to (i) pioneer the use of TDDFT for heterogeneous systems and (ii) to determine whether any information useful to our experimentalist colleagues could be obtained. The figure below shows a selection of the models, varying in size from 38 atoms in gas-phase MB^+ to 480 in a hydrated kaolinite/MB^+ system.

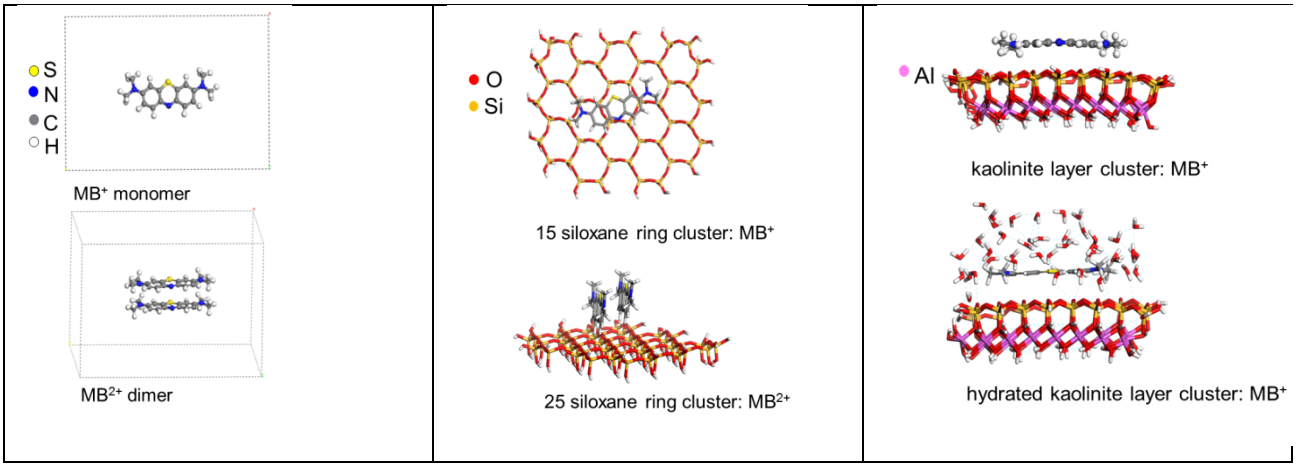

Figure 3.5.1: A selection of the models, varying in size from 38 atoms in gas-phase MB^+ to 480 in a hydrated kaolinite/MB^+ system.

All calculations were limited to a single sampling point (gamma) due to the current implementation of TDDFT within CASTEP, limiting the clay mineral layers to clusters rather than periodic bulk systems. The smallest calculation employed 16 cores for relaxation of the atomic positions and the largest 128 for the TDDFT properties task following relaxation of the atomic positions. Finding the ground state geometry was comparably a longer task than the TDDFT calculation, which was relatively quick (days rather than weeks) but comparably more demanding on memory (10's of Gb rather than 100's of Mb). This work is currently on-going and is part of a larger study involving Sebastian Metz and Tom Keal in the Chemistry Group of SCD. We presented a poster on our current results at the CCP5 meeting, at Lancaster University, September 2015 and intend to publish the whole study early next year.

References

[1] Clark, S.J., Segall, M.D., Pickard, C.J., Hasnip, P.J., Probert, M.J., Refson, K., and Payne, M.C. (2005) Castep v5.0. Zeitschrift für Kristallographie, 220, 567–570

3.6 Quantitative plasma wakefield diagnostic using single shot laser probe pulse

M. F. Kasim[1], J. Holloway[1], L. Ceurvorst[2], M. C. Levy[2], N. Ratan[2], J. Sadler[2], R. Bingham[3,4], P. N. Burrows[1], R. Trines[3], M. Wing[5], P. A. Norreys[2,3]

[1]*John Adams Institute, Denys Wilkinson Building, Keble Road, Oxford OX1 3RH, United Kingdom.*
[2]*Clarendon Laboratory, Department of Physics, University of Oxford, Parks Road, Oxford OX1 3PU, United Kingdom.*
[3]*STFC Rutherford Appleton Laboratory, Chilton, Didcot OX11 0QX, United Kingdom.*
[4]*Department of Physics, University of Strathclyde, Glasgow G4 0NG, United Kingdom.*
[5]*Department of Physics and Astronomy, University College London, Gower Street, London WC1E 6BT, United Kingdom.*

Plasma wakefield accelerator is a promising technology that could revolutionise particle accelerator technology. The electric field in plasma wakefield can have a value around 10-100 GV/m, which is about 3 orders of magnitude higher than in the conventional accelerators. In a plasma wakefield accelerator, a driver is fired into ionised gas and drives waves in plasma that are called wakefield. This wakefield then provides an electric field that can be used to accelerate particles.

One challenge in plasma wakefield accelerator development is the inadequacy of techniques to diagnose the wakefield itself in real experiments. To address this problem, we proposed a novel solution to quantitatively diagnose the plasma wakefield using a single shot laser probe pulse. The probe pulse is fired to cross the wakefield with an oblique angle. When the probe pulse crosses the wakefield, it experiences frequency and phase shift because of an effect called photon acceleration. By measuring the frequency or phase shift of the probe pulse, one can apply an inverse transformation to obtain the density profile of the wakefield. From the density profile, one can then infer other parameters such as wavelength, radius, and on-axis amplitude of the wakefield.

We used SCARF to run 3D simulations using particle-in-cell (PIC) code, OSIRIS, to check the accuracy of this measurement technique. We also performed a parameter scanning to see the limitations of this technique. In the simulations, we obtained 2 profiles: (1) electron density profile and (2) frequency shift profile of the probe pulse. From the frequency shift profile, we then applied a modified inverse Abel transformation to get the 'measured' electron density profile. The 'measured' electron density profiles are compared with the electron density profiles obtained directly from the simulation. The comparison results are shown in Fig. 1. The details of the transformation and complete results of the simulation are published in Ref. [2].

Using the results from SCARF, this work successfully gets an experimental slot of 12 weeks in Astra laser facility starting May 2016 as a proof-of-concept of this technique. Besides that, this work is also going to be integrated in AWAKE experiment [3], a proton-driven plasma wakefield experiment, starting on October 2016 at CERN, Switzerland.

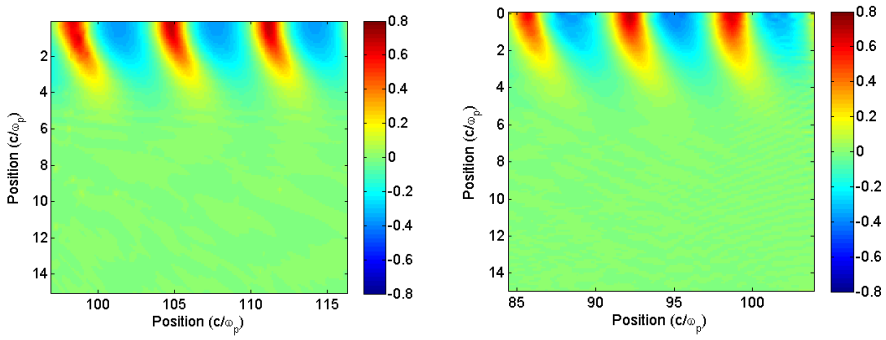

Figure 3.6.1: The comparison between actual electron density profile (left) obtained directly from the simulation and the measured electron density profile (right) calculated from the frequency shift of the laser probe pulse.

References

[1] S. P. D. Mangles, C. D. Murphy, Z. Najmudin, A. G. R. Thomas, J. L. Collier, A. E. Dangor, E. J. Divall, P. S. Foster, J. G. Gallacher, C. J. Hooker, *et al.*, Nature **431**, 535 (2004).

[2] M. F. Kasim, J. Holloway, L. Ceurvorst, M. C. Levy, N. Ratan, J. Sadler, R. Bingham, P. N. Burrows, R. Trines, M. Wing, P. A. Norreys, Phys. Rev. ST Accel. Beams **18**, 081302 (2015).

[3] AWAKE Collaboration, AWAKE Status Report, CERN-SPSC-2014-026; SPSC-SR-143 (2014).

3.7 A rigorous quantum-mechanical treatment of radiation induced atomic dynamics in crystalline systems

Leonardo Bernasconi Theoretical and Computational Physics Group STFC Scientific Computing Department
José Brandao-Neto Macromolecular Crystallography Group Diamond Light Source Ltd

Ab initio molecular dynamics (AIMD) [1] is a well established and widely used set of computational techniques whose aim is to account for the microscopic dynamics of atoms and molecules by explicitly considering the influence of electronic relaxation during the nuclear motion. In essence, quantum-mechanical forces between atoms are determined by solving a many-body Schrödinger equation (*e.g.* within the density-functional theory approximation). These quantum-mechanical forces are then used to propagate the atoms as classical particles in a Newtonian framework. AIMD, first proposed by Car and Parrinello in 1985, [2] has revolutionized research in solid state physics, chemistry and the biological sciences, because of its ability to account, for instance, for bond breaking and formation during chemical reactions, structural relaxation in complex macromolecular systems and phase transitions in condensed phases.

One of the most challenging and potentially far reaching developments in AIMD in recent years has been the generalization of standard (ground state) dynamics to the treatment of electronically excited states. AIMD-based methods have been proposed to account for the nuclear relaxation of molecular systems in the presence of electromagnetic radiation (IR, visible light, UV, as well as ionizing radiation). In a typical UV, visible or X-ray absorption experiment, the motion of the electrons in a sample is influenced by the external radiation, and electrons oscillate at characteristic frequencies determined by the rules of quantum mechanics. Some of these oscillatory modes correspond to transitions between the ground state and an electronically excited state, and result in well defined signatures in the absorption spectrum. Since the system is now no longer in its ground state, the quantum mechanical forces acting on the atoms differ from those of the unperturbed sample, and the dynamics of the nuclei deviates from a standard AIMD trajectory. The problem of determining the correct trajectory in the presence of radiation is complicated by the fact that several excited states can contribute to the dynamics, either simultaneously or at different times.

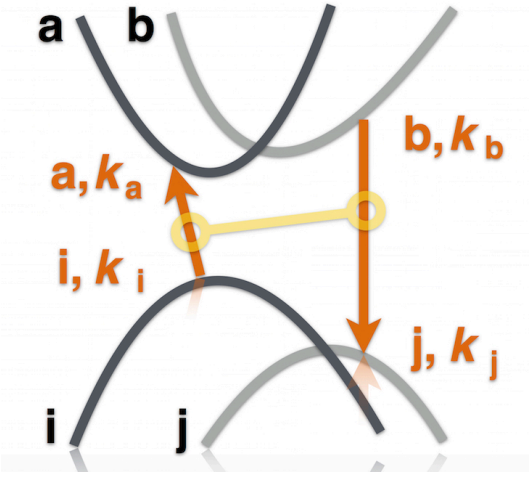

Figure 3.7.1: Electronic transitions between energy bands in a crystalline system and exciton formation through the coupling of elementary excitations.

The problem is even more complicated in extended systems (Figure 3.7.1), like crystals, in which many-body states (**excitons**) can be created by photo-excitation through the coupling of several elementary transitions between occupied (**i**, **j**) and virtual (**a**, **b**) energy bands at different values of the crystal quasi-momentum **k**. Excitons are localized bound electron-hole pairs, which can interact with the atomic lattice and perturb its equilibrium geometry and its dynamics. The ability to account for the formation of excitons in crystals, amorphous systems, molecular liquids and macromolecules from first principles is of fundamental importance in the accurate first-principles modelling of their response to electromagnetic radiation.

Work carried out within the TCP group at the Rutherford Appleton Laboratory and Daresbury Laboratory over almost ten years has led to the development of very accurate and efficient methods based on time-dependent density-functional theory (TD-DFT) [3, 4] to describe excitons in semiconductors and insulators. [5, 6] These capabilities have been implemented in the CRYSTAL software (http://www.crystal.unito.it/), one of the most powerful electronic structure codes currently available. CRYSTAL is also one of the most widely used codes on the SCARF cluster, and a large component of the parallelisation and optimisation of the excited state capabilities in the latest release of the code (CRYSTAL14) has been carried out on this platform.

We are currently developing an approach to study the relaxation of a crystal lattice at finite temperature after the formation of an exciton by UV light absorption. Our first application of this method has been on quasi one-dimensional polymeric systems, in the crystalline state. ***Trans*-polyacetylene** (Figure 3.7.2a) is a particularly interesting example in which a singlet exciton interacts with the atomic lattice to create localized topological defects (**solitons**, Figure 3.7.2b), which, at room temperature, propagate along the polymeric chain transporting charge and/or spin. **[7]** Although the existence of solitons in polyacetylene has been predicted in the past based on semi-empirical models, our study represents the first attempt to account for their formation and real-time dynamics using a first-principles (parameter free) quantum mechanical method.

Our work demonstrates the existence of interactions between solitons determined by the correlation in the motion of the photoexcited electrons and holes, which leads to the appearance of exotic phenomena like 2-bounce resonances (Figure 3.7.2c), indicative of chaotic propagation of soliton pairs at short distances, and to soliton condensation at low temperatures (Figure 3.7.2d). Polyacetylene is the prototype of an important class of materials known as **conductive polymers**, with applications in photovoltaics, optoelectronics, nonlinear optics, and electromagnetic shielding.

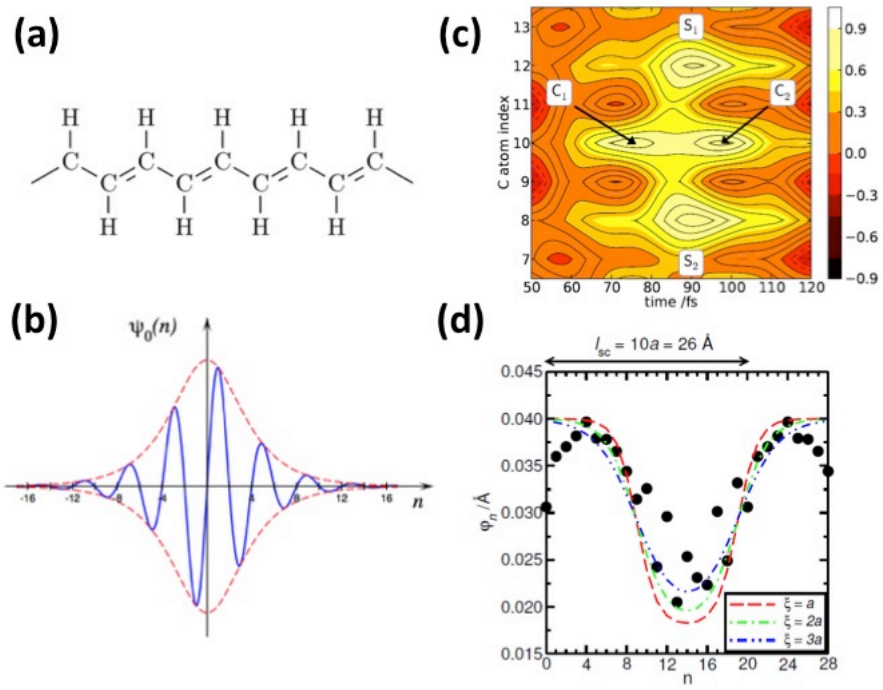

Figure 3.7.2: (a) Structure of *trans* polyacetylene; (b) a soliton wavefunction; (c) 2-bounce collision of solitons; (d) soliton condensation into a bound polaronic pair.

A second example of the application of our TD-DFT excited-state dynamics approach is in the study of **X-ray induced radiation damage** in macromolecular crystals. In collaboration with the Macromolecular Crystallography Group at the Diamond Light Source, we have examined the atomic level dynamics of crystals of **beeswax** analogues (*n*-eicosane, Figure 3.7.3a), a material recently proposed as a calibration standard for X-ray crystallography instrumentation. [8]

Understanding at an atomistic level the origin and dynamics of formation of structural defects in samples of organic and biological molecules (proteins, DNA, *etc.*) exposed to ionising radiations has important implications in the resolution of X-ray structures as well as in the study of the physiological mechanisms leading to mutations in living cells. The applications of quantum mechanical methods to this field has so far been extremely limited, because of the structural complexity and size (*e.g.* in terms of number of atoms per unit cell) of the systems of interest.

Our simulation indicates that X-ray absorption induces permanent changes in the crystalline structure, which are associated with a local distortion of *n*-eicosane chains. This distortion is caused by the atoms moving to screen the Coulomb attraction between the electron-hole pair created by X-ray excitation. This study demonstrates the existence of a new class of photogenerated defects in organic crystals, which are created over timescales of the order of a few picoseconds and can lead to the eventual degradation of the sample in an X-ray beam. The simulation was carried out entirely on SCARF and it took over 6 months (on 64 processors) to complete.

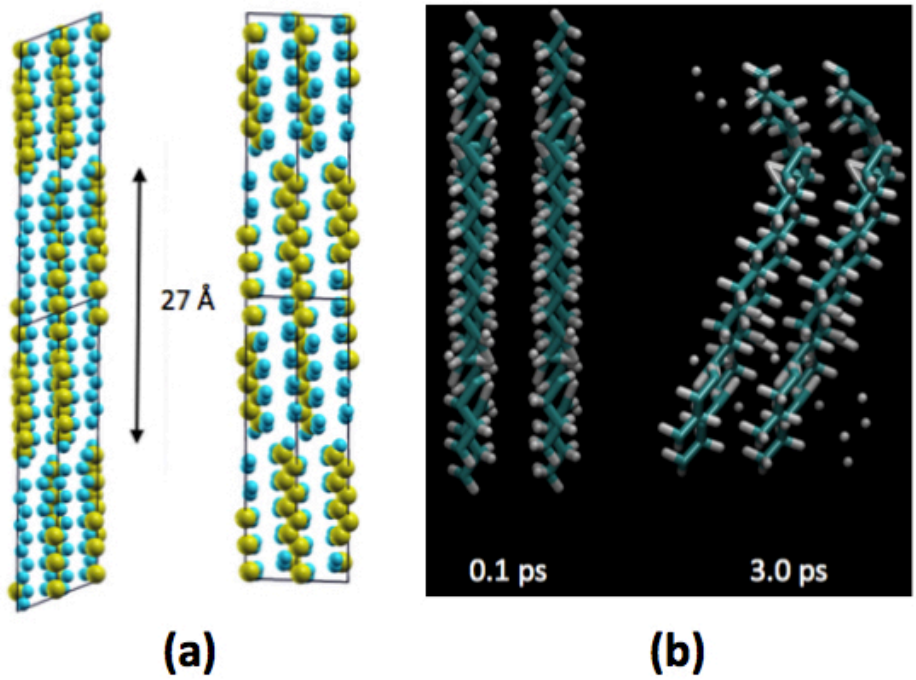

Figure 3.7.3: (a) Crystal structure of *n*-eicosane; (b) structural relaxation of the crystal 0.1 ps and 3.0 ps after irradiation with X-rays.

References

[1] D. Marx and J. Hutter, *Ab initio molecular dynamics: Theory and Implementation*, In: J. Grotendorst (ed.) Modern Methods and Algorithms of Quantum Chemistry, p. 301. John von Neumann Institute for Computing, Jülich (2000).

[2] R. Car and M. Parrinello, *Unified Approach for Molecular Dynamics and Density- Functional Theory*, Phys. Rev. Lett. 55, 2471 (1985).

[3] L. Bernasconi, S. Tomić, M. Ferrero, M. Rérat, R. Orlando, R. Dovesi, N. M. Harrison, *First-principles optical response of semiconductors and oxide materials*, Phys. Rev. B **83**, 195325 (2011).

[4] L. Bernasconi, R. Webster, S. Tomić and N. M. Harrison, *Optical response of extended systems from time-dependent Hartree-Fock and time-dependent density-functional theory*. J. Phys.: Conf. Ser. 367, 012,001 (2012).

[5] S. Tomić, L. Bernasconi, B. Searle and N. M. Harrison, *Electronic and optical structure of wurtzite $CuInS_2$*, J. Phys. Chem. C 118, 14478 (2014).

[6] R. Webster, L. Bernasconi and N. M. Harrison, *Time-dependent density-functional theory description of exciton binding in alkali halide crystals: The role of Hartree-Fock exchange*, J. Chem. Phys. 142, 214705 (2015).

[7] L. Bernasconi, *Chaotic soliton dynamics in photoexcited trans-polyacetylene*, J. Phys. Chem. Lett. 6, 908 (2015).

[8] L. Bernasconi and J. Brandao-Neto, *Radiation damage in X-ray crystallography: A quantum-mechanical study of photoinduced defect formation in beeswax-analogue n-eicosane crystals* , Manuscript submitted (2015).

3.8 Automatic Setup of Alchemical Free Energy Simulations

Hannes Loeffler (SCD)

Being able to compute the free energy can help tremendously in understanding fundamental processes in nature. For example, the free energy of binding can be estimated for a ligand–receptor through various free energy techniques. Knowledge of this quantity enables the scientest to decide which potential drug molecules are most likely to bind to a target and are thus candidates for future pharmaceuticals. It is therefore easy to understand that accurate calculation of the free energy is often called the "holy grail" of computational chemistry.

I currently develop *FESetup* which is an automatic setup tool for relative alchemical free energy simulations. This is carried out in collaboration with Julien Michel (Edinburgh) and Christopher Woods (Bristol) for the core–support of CCPBioSim. *FESetup* has been presented in a LunchtimeByte at the annual CCPBioSim conference 2015 in Leeds, at the FEW Free Energy Workshop 2015 in poster format in Muenster, Germany and will also centrally feature (invited talk) at the CECAM workshop "Macromolecular simulation software workshop" in October 2015 in Juelich, Germany. A manuscript describing the software in detail is currently under review.

A current project is to evaluate various simulation software in being able to reproduce the relative free energy of hydrationn of small organic molecules. Tested software is AMBER, GROMACS, CHARMM and Sire. It has not been established thus far if these programs are actually able to produce comparable free energies (within statistical errors). Data on this is currently compiled and will be published in the near future. The study is carried out in collaboration with Julien Michel (Edinburgh), David Mobley (UC Irvine, USA) and Benoit Roux (University of Chicago, USA).

SCARF is an excellent platform for carrying out small scale free energy simulations. The platform allows to run many thousands of jobs in a minimum amount of time and also enables high throughput. Each simulation window would typically run on about 4–16 cores and we need to compute several hunreds to thousands of them. Many other HPC facilities in the UK are geared towards highly scalable problems and would thus not allow us to do this kind of work (restrictions through queuing policies or not allowing this type of simulation at all).

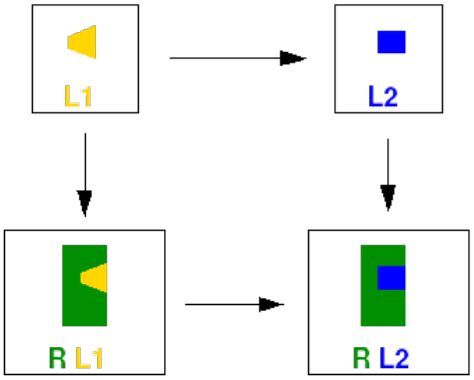

Figure 3.8.1: A typical thermodynamical cycle to compute free energies of binding for a target receptor. It is computationally much more efficient to simulate along horizontal lines. Transformations from L1 to L2 would be usually be computed in several steps ("windows").

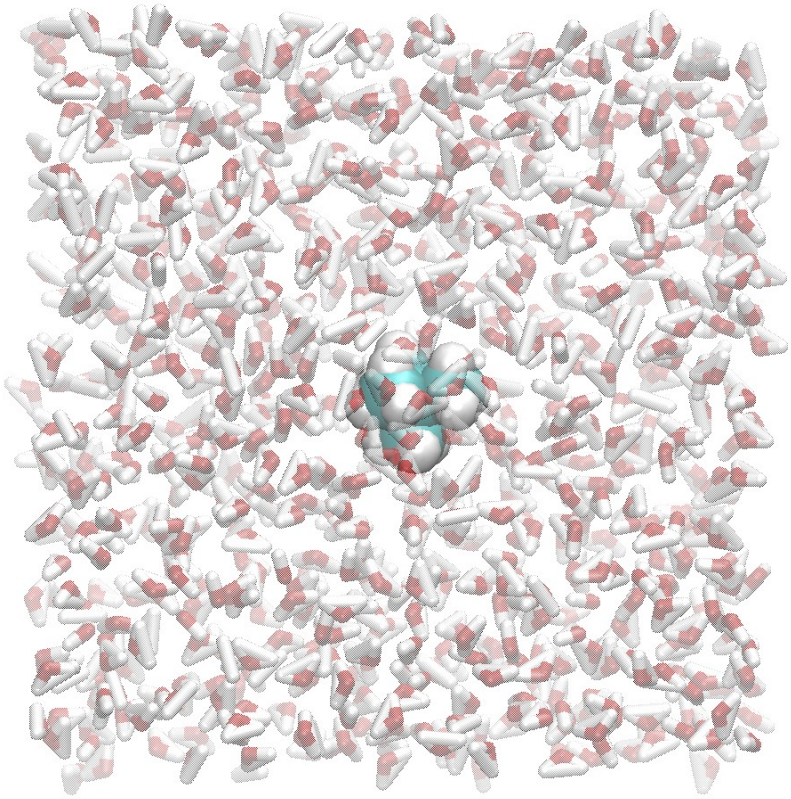

Figure 3.8.2: A small organic molecule in solution will be transformed into another one by means of thermodynamic integration.

3.9 Monte Carlo modelling of TOSCA neutron spectrometer: an update

R.S. Pinna (ISIS and Università degli Studi di Milano-Bicocca), S. Rudic (ISIS), S.F. Parker (ISIS), G. Gorini (Università degli Studi di Milano-Bicocca) and F. Fernandez-Alonso (ISIS and University College London)

TOSCA is a broadband, indirect-geometry inelastic neutron spectrometer optimised for high-resolution spectroscopy up to energy transfers of ca. 500 meV in neutron-energy loss. Its sample position sits at 17 m from a room-temperature water moderator. When TOSCA was constructed, neutron guides were ineffective for the relatively hot neutrons required. Nevertheless, neutron guide technology has greatly improved and TOSCA current need is for greater sensitivity via provision of a guide in the primary spectrometer, thus a validated Monte Carlo model is crucial to probe this upgrade.

In the past, the work has proceeded in the design of the TOSCA neutron guide (see previous SCARF report for additional details) and explored in-depth features of the spectrometer by use of Monte Carlo calculations. To achieve these goals, a deep refinement of the current Monte Carlo model was required as well as a new modelling of the full spectroscopic capabilities of TOSCA. The simulations were performed on SCARF cluster, we used up to 128 cores and the typical duration was approximately 12 hours. Furthermore, in situ experiments were performed for a deeper benchmarking of the calculations in order to confirm the full validity of the model.

According to the calculations, see Figure 3.9.1 and 3.9.2, the upgrade of the TOSCA beamline provides a neutron flux gains for the optimal configuration of 50 and 3 for the highest and lowest incident wavelengths available on the instrument, respectively. Use of a high-m guide (m>4) close to the source ensures reasonable gain factors above 20 meV. The spectral resolution of the instrument around the elastic line appears largely insensitive to a rather substantial increase in the m-number of the guide. These results are to be taken as a lower limit, given the linear dependence of beam divergence on both incident wavelength and m-number. Hence, it appears that the predicted gains provided by the guide are not accompanied by a concomitant degradation of the spectroscopic capabilities presently afforded by TOSCA.

The latest calculations were aimed to a deep refinement of the guide geometry, in order to improve further the flux and to minimize the inhomogeneities in the beam profile at both TOSCA and INES sample position.

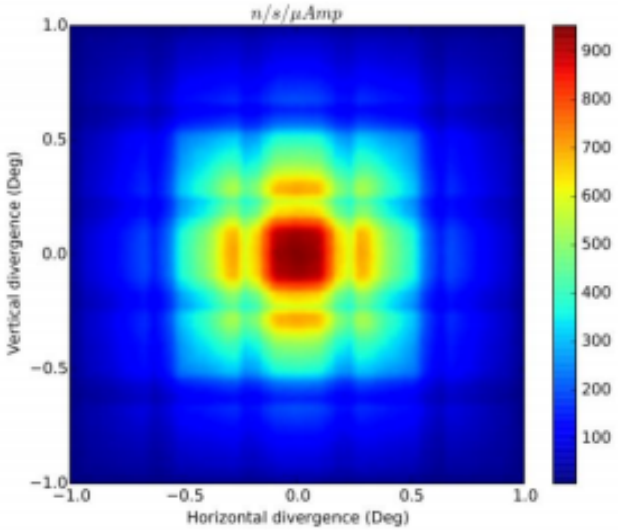

Figure 3.9.1: Example of the neutron divergence profile through the Tosca sample plane, calculated with the McStas Monte Carlo software on SCARF

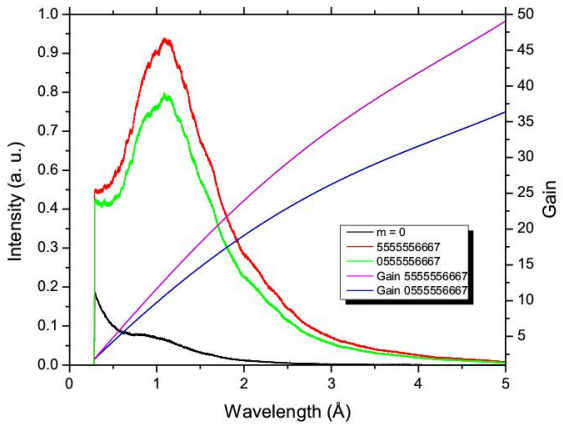

Figure 3.9.2: Wavelength spectrum and related gain at TOSCA sample position for the optimal guide configuration (shown in legend), the configuration without the first guide is included as well. The actual beamline configuration (m = 0) is plotted as a term of comparison. The calculations were performed with the McStas Monte Carlo software on SCARF.

3.10 Work performed on SCARF

Pietro Bonfà[(1)], Roberto De Renzi[(1)]

[(1)] Department of Physics and Earth Sciences, University of Parma, Italy

Our work with SCARF was mainly devoted to the analysis of muon sites and muon induced perturbations with first principles Density functional theory (DFT) simulations. The use of *ab initio* methods to complement and support the analysis of muon spin rotation and relaxations spectroscopy (μSR) has attracted a renewed interest during the last decade.

This is mainly due to the effectiveness of this approach in providing precious information regarding the muon embedding process which are often necessary to deepen the quantitative analysis of the experimental data. In this context, DFT was mainly used to provide *ab initio* predictions of the muon embedding sites and to evaluate the effect that this positively charged impurity produces in the hosting material.

We validated our method on Cu and MnSi [1] and then focused our attention on $LaCrGe_3$ and MnGe. Here we will only describe the results obtained for last two compounds.

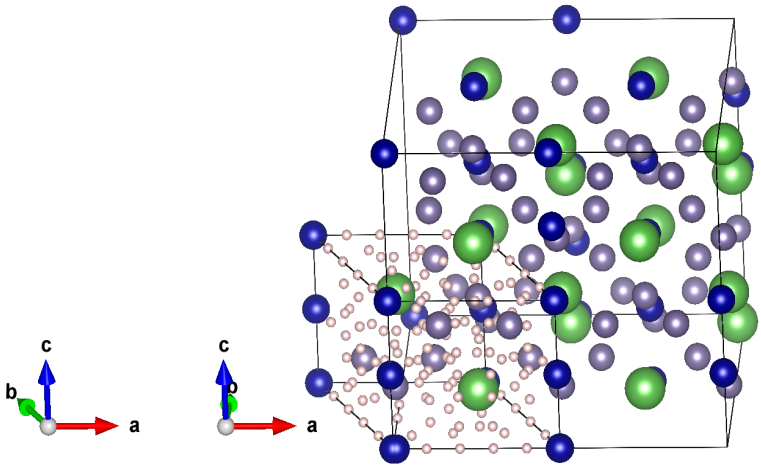

Figure 3.10.1: The grid of interstitial positions used to identify the muon embedding site in $LaCrGe_3$. The supercell used for the simulations is shown as well.

$LaCrGe_3$ is an hexagonal perovskite-type compound which displays unusual magnetic properties as a function of applied pressure. The experimental data, acquired at PSI, are not sufficient to describe the new magnetic phase which develops as a function of applied pressure, and, in order to distinguish between the possible long range magnetic orders, the knowledge of the interstitial position occupied by the muon is required.

The muon site was located with the procedure described in Refs. [1,2] . We identified various candidate sites starting from the grid of interstitial position showed in Fig. 3.10.1. Only one stable position was eventually found.

Another successful result was obtained in MnGe, a compound which is supposed to display a skyrmionic phase in a rather large part of its electronic phase diagram [3].

In order to identify the skyrmionic phase with μSR, an accurate description of the muon embedding process and of its effect on the hosting system is necessary. To this aim, we identified the muon site in MnGe and we estimated the contact hyperfine field contribution to the μSR signal.

Fig. 3.10.2 shows the stable position of the muon in MnGe and the probability density of the μ^+ obtained from the solution of the Schrodinger equation of the muon in the potential produced with the double adiabatic approximation [1].

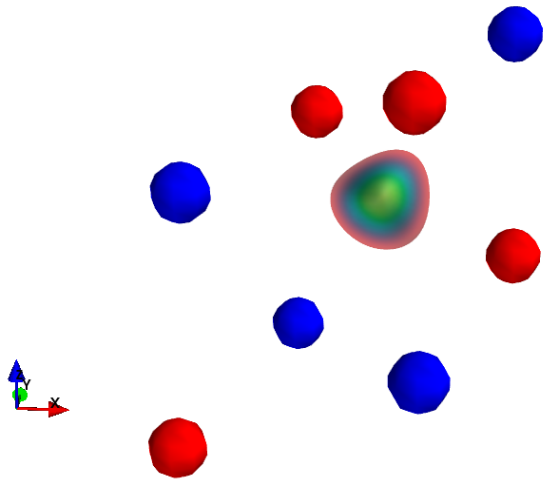

Figure 3.10.2: The probability density of the muon is depicted with a color gradient. Red spheres represent Mn, blue spheres represent Ge.

References

[1] Efficient and Reliable Strategy for Identifying Muon Sites Based on the Double Adiabatic Approximation, P. Bonfà, F. Sartori, and R. De Renzi, J. Phys. Chem. C **119**, 4278 (2015)

[2] Quantum states of muons in fluorides, J. S. Möller, D. Ceresoli, T. Lancaster, N. Marzari, and S. J. Blundell, Phys. Rev. B **87**, 121108R (2013)

[3] Possible skyrmion-lattice ground state in the B20 chiral-lattice magnet MnGe as seen via small-angle neutron scattering, N. Kanazawa, J.-H. Kim, D. S. Inosov, J. S. White, N. Egetenmeyer, J. L. Gavilano, S. Ishiwata, Y. Onose, T. Arima, B. Keimer, and Y. Tokura. Phys. Rev. B **86**, 134425 (2012)

3.11 Two-dimensional Cs-vacancy superstructure in iron-based superconductor $Cs_{0.8}Fe_{1.6}Se_2$

D.J. Voneshen (RHUL/ISIS), D.G. Porter (DLS), K. Refson (RHUL/STFC), J.P. Goff (RHUL)

The new family of iron-based superconductors $A_xFe_{2-y}Se_2$, where A = K, Rb and Cs [1] show some remarkable differences to the iron-pnictide high-Tc's [2,3]. Superconductivity in $K_xFe_{2-y}Se_2$ appears to coexist with antiferromagnetism with an unusually high ordering temperature $T_N \sim 559$ K and a large ordered moment of about 3.3μB per Fe [4]. This magnetic state is commensurate with a $\sqrt{5}\times\sqrt{5}$ superstructure of ordered Fe vacancies at $y = 0.4$ [5]. A 2D $\sqrt{2}\times\sqrt{2}$ superstructure has also been observed in some samples and is thought to be closely related to the superconducting phase [6].

While several structures had been proposed to explain the $\sqrt{2}\times\sqrt{2}$ superstructure all had been 3D in nature and thus unable to explain the rods of scattering seen with both neutron and x-ray diffraction. By combining high resolution x-ray (on I16 at Diamond Light Source) and neutron diffraction (on SXD at ISIS) it was possible to separate and refine the compositions of $\sqrt{5}\times\sqrt{5}$ and $\sqrt{2}\times\sqrt{2}$ phases independently. This new analysis indicated that the $\sqrt{2}\times\sqrt{2}$ phase consisted solely of Cs vacancies with $x = 0.5$. First principles calculations performed on SCARF using the CASTEP code showed that such a system of Cs vacancies would be expected to order within the a-b plane but crucially not between the planes explaining the observed 2D order.

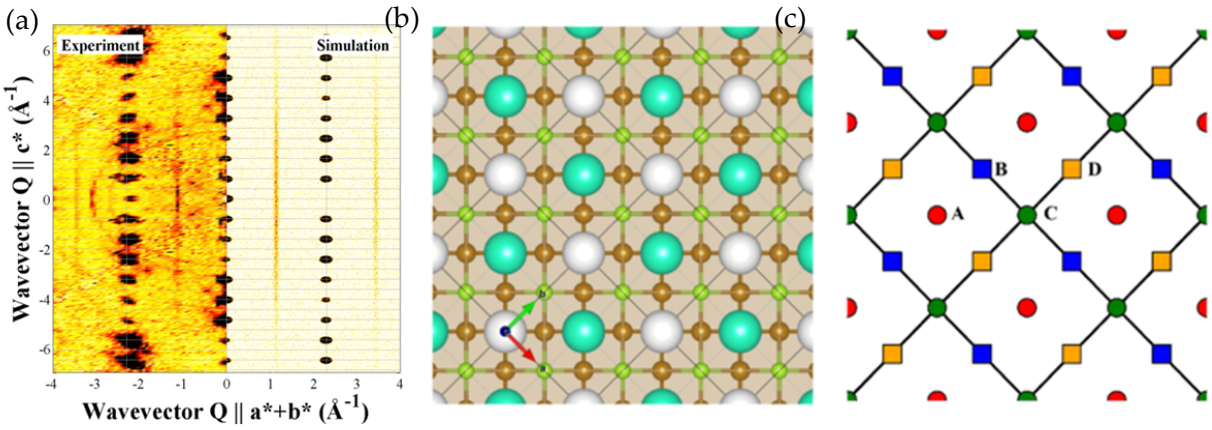

Figure 3.11.1: a) The Bragg rods observed on SXD and the calculated scattering from a 2D Cs vacancy superstructure. b) The in-plane Cs superstructure with Cs shown in light blue and vacancies in white. c) The possible sites that each Cs layer can sit in, circles and squares indicate the two different layers.

This work has been published in PRB (DOI:10.1103/PhysRevB.91.144114), presented at the Advances in Modern Magnetic Materials, Symposium on Energy Challenges & Mechanics conferences and mentioned by ISIS director R. McGreevy as a science highlight during his July 2015 staff talk. Furthermore on the basis of calculations performed on SCARF two successful beam time applications to the ILL were put in (for the instruments IN20 and IN8) as well as a successful 10,000 KAu grant proposal for the EPSRC supercomputer ARCHER which we are currently writing up.

References

[1] J. Guo et al., Phys. Rev. B 82, 180520(R) (2010)
[2] Y. Zhang et al., Nature Materials 10, 273 (2011)
[3] J.T. Park et al., Phys. Rev. Lett. 107, 177005 (2011)
[4] W. Bao et al., Chin. Phys. Lett. 28, 086104 (2011)
[5] P. Zavalij et al., Phys. Rev. B 83,132509 (2011)
[6] M. Wang el al., Phys. Rev. B 84, 094504 (2011)

3.12 Guiding Laser-Generated Fast Electrons with a Transverse Resistivity Gradient that is Inversely Conically Tapering

A.P.L.Robinson and H.Schmitz, STFC Central Laser Facility

Ultra-intense laser-solid interactions are well known to involve the coupling of a substantial fraction of laser energy into multi-MeV 'fast' electrons. These have long ranges in solid material and carry high energy density and high current density. Their propagation is strongly influenced by self-generated electric and magnetic fields. Understanding their propagation will be essential for developing applications : fast electron driven ion accelerators, x-ray sources, and neutron sources. In addition to this, advanced laser-fusion concepts have been proposed that exploit fast electron beams as ignitor elements.

In this study carried out using the SCARF-LEXICON resources in the 14/15 period we studied a variant of schemes that exploit deliberately engineered resistivity gradients by constructing targets from different materials. The main scheme that we considered can be described as the 'inverse conical taper' configuration, which is described in Fig.3.12.1 below. The key feature is a truncated cone whose radius increases as one moves along the axis away from the source.

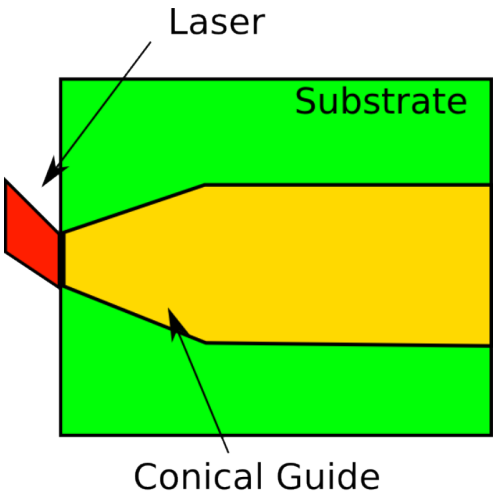

Figure 3.12.1: Inverse conical taper configuration

The inverse conical taper configuration exploits the fact that an oblique deflection of a fast electron from the magnetic fields that one expects to be generated at the guide-substrate interace will lead to a reduction in the propagation angle of the fast electron by twice the half-angle that the cone subtends. This means that the angular distribution of the fast electrons should be shrunk by the inverse conical taper.

In figure 3.12.2 we show results from calculations that show the efficacy of the inverse conical taper in reducing the angular distribution of a fast electron beam. This is compared to both a uniform substrate, a straight wire, and inverse conical tapers of different half-angles.

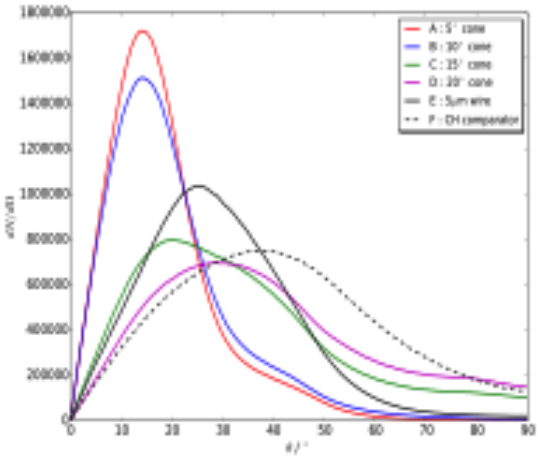

Figure 3.12.2: Angular distribution

As this effect on the angular distribution can improve the prospects for confining the fast electrons in a straight wire, the inverse conical taper can be used as a 'front end' for a straight wire in order to substantially improve heating of the wire. This improvement is shown in figure 3.12.3, where we show plots of background electron temperature in the mid-plane of Zephyros simulations using a straight wire with an inverse conical taper front end. The top left and bottom right correspond to the ICT targets with low taper angles. There is huge increase in heating compared to the comparator target.

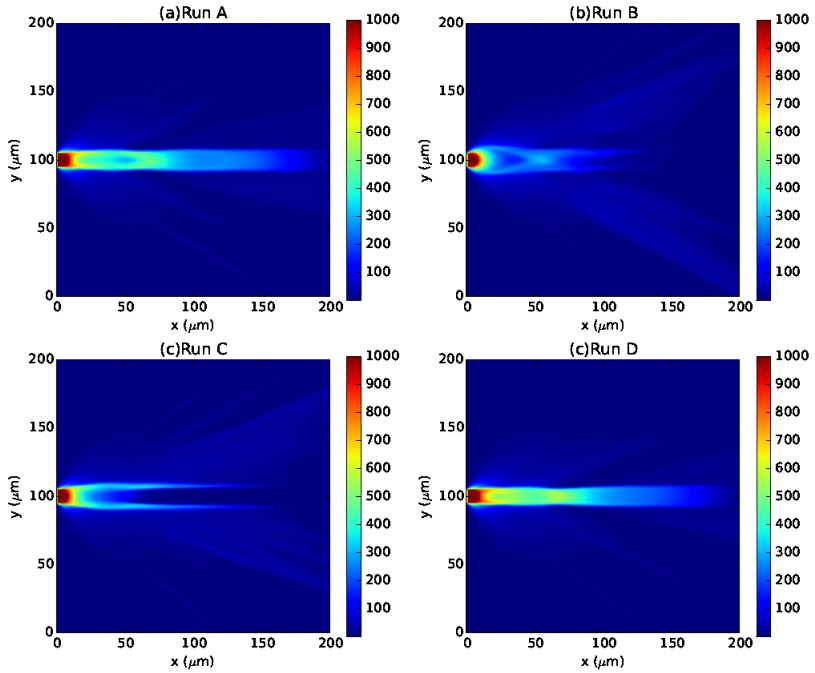

Figure 3.12.3: Background electron temperature in the mid-plane of Zephyros simulations using a straight wire with an inverse conical taper front end

In summary we have used the CLF's Zephyros code to study the effect of inverse conical tapers on fast electron transport guided by resistivity gradients. The use of the ICT can have a dramatic effect on the fast electron angular distribution and the heating of the background material.

3.13 Work performed on Scarf 2014-2015

Robbie Scott, Plasma Physics Group, Central Laser Facility.

I have performed a wide range of simulation work has been performed on Scarf over the last year including both personal research and simulations for users of the CLF from universities.

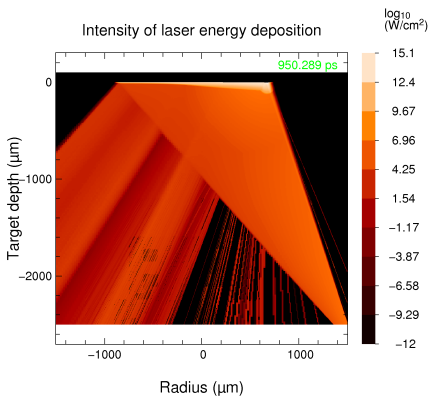

Figure 3.13.1: A radiation-hydrodynamics simulation of the Astra-Gemini laser driving a strong shock into a Silicon wafer.

Using the laser-wakefield electron acceleration technique, physicists from Imperial College London have devised a new way of creating very short, intense, bunches of coherent x-rays. As the coherent bunches pass through matter, the x-rays move out of phase with one another. This de-phasing can occur either because materials have differing refractive index, or because the rays pass through differing path lengths. Either way, the de-phasing can greatly enhance the image contrast in comparison to conventional x-ray imaging based on absorption. This technique is called phase contrast imaging, and may be of great benefit to medicine. Running on Scarf, the 3 dimensional radiation-hydrodynamics code FLASH has been used in the design and interpretation of a phase contrast imaging experiment performed on the Astra-Gemini laser at the Central Laser Facility.

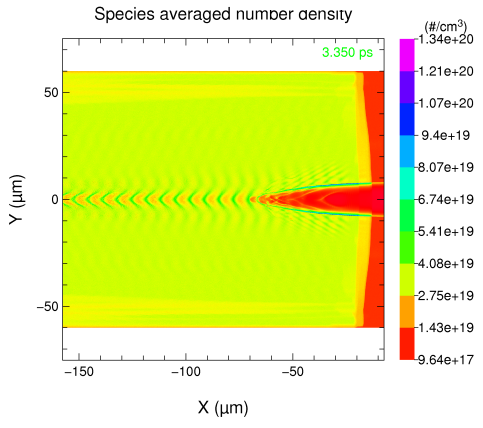

Figure 3.13.2: Particle-in-cell modelling of electron acceleration via the laser-wakefield technique enables the key physics to be understood – aiding the design of the next generation of particle accelerators.

University of Oxford researchers use the Central Laser Facility's Astra-Gemini laser to accelerate electrons to GeV energies using the 'plasma wakefield' technique, which, if perfected, will

revolutionise future accelerator technology. Their experimental data showed some encouraging, but puzzling, results. Understanding this complex interaction required extensive use of the Scarf cluster to run a combination of the Particle-in-cell code EPOCH to capture the complex kinetics of the laser-plasma interaction, followed by radiation-hydrodynamics modelling of the hydrodynamic plasma expansion with the FLASH code, then finally a second particle-in cell modelling stage of the plasma wakefield generation. Using scarf it has been possible to gain a full understanding of the physics involved, enabling researchers to better design the next generation of electron accelerators.

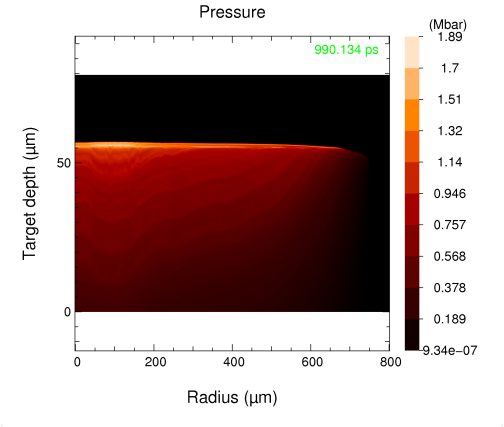

Figure 3.13.3: Simulations of the Vulcan laser at the Central Laser Facility driving a Megabar shock into Iron – recreating the conditions in the Earth's core.

Researchers from Queens University Belfast have used the Central Laser Facility's Vulcan laser to compress matter to extreme states – similar to those found in the earth's core. Running on Scarf, the FLASH radiation-hydrodynamics code has been used to model the laser-plasma interactions and the conditions generated, enabling researchers to better understand their experimental data and the complex states of matter found in planetary cores.

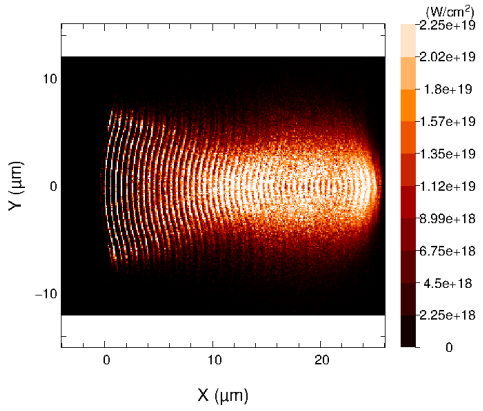

Figure 3.13.4: A convergent beam of fast-electrons modelled using the Particle-in-cell code EPOCH on Scarf.

Particle-in-cell modeling using the code EPOCH on the Scarf clusters, has been used to explore the feasibility of an innovative new laser-plasma interaction geometry. This work has shown for the first time that it is possible to create a convergent fast-electron (1-3MeV) beam from the laser-plasma interaction. The extremely high-current fast-electron beam can be focused at a specified depth within a solid target. This work may be important in the development of the fast-ignition inertial confinement fusion concept, which proposes the use of a beam of fast-electrons to heat compressed Deuterium and Tritium fuel to initiate thermonuclear fusion.

3.14 Explaining the Mechanical Mechanisms of Zeolitic Metal-Organic Frameworks: Revealing Auxeticity and Anomalous Elasticity

Matthew R. Ryder and Jin-Chong Tan, *Department of Engineering Science, University of Oxford*

Zeolitic imidazolate frameworks (ZIFs) represent a major subfamily of metal-organic frameworks (MOFs). ZIFs combine the thermal and chemical stability of inorganic zeolites with the rich topological diversity and pore size tunability characteristic of MOFs. The structures of ZIFs comprise of tetrahedral metal centres (Mn^{+} = Zn^{2+}, Co^{2+}, Li^{+}, B^{3+}) bridged by imidazolate-derived linkers.

In this work, we set out to explore the mechanical bounds of ZIFs. In particular, we focused on the elastic properties of four ZIF structures, ZIFs-1 to -4, all of which feature an identical chemical composition $Zn(Im)_2$ where its divalent Zn^{2+} cations are coordinated to unsubstituted imidazolate linkers [Im = $C_3H_3N_2^-$]. However, their crystal symmetries, network topologies, geometrical parameters and physical properties are remarkably different. Using *ab initio* theoretical calculations performed on the SCARF cluster, we demonstrated that the elastic characteristics and structure–property relationships of ZIF-1 to ZIF-4 are distinctive to each framework. We have uncovered a number of previously unreported elastic anomalies of ZIFs, for which we have identified the molecular origins and their physical significance.

The comprehensive elastic properties of ZIF-1 to ZIF-4 were computed using density functional theory (DFT). We employed the periodic CRYSTAL14 code to calculate the single-crystal elastic coefficients (C_{ij}) at the B3LYP level of theory. We elucidated the anisotropic mechanical response with respect to the directionally dependent Young's and shear moduli properties. Our theoretical results suggested that ZIF-3 adopting a **dft** topology has an extremely low shear resistance (G_{min} = 0.1 GPa), which is also underpinning the flexible mechanism responsible for its negative Poisson's ratio (auxetic ν_{min} = −0.43). Interestingly, we identified that ZIF-1, ZIF-2, and ZIF-4 could exhibit a nearly zero Poisson's ratio for certain crystal orientations, which is reminiscent of a rare "cork-like" phenomenon where there is practically no lateral deformation corresponding to an applied axial strain. Furthermore, we determined the bulk moduli and linear compressibilities, alongside the averaged elastic properties of the ZIF polycrystals.

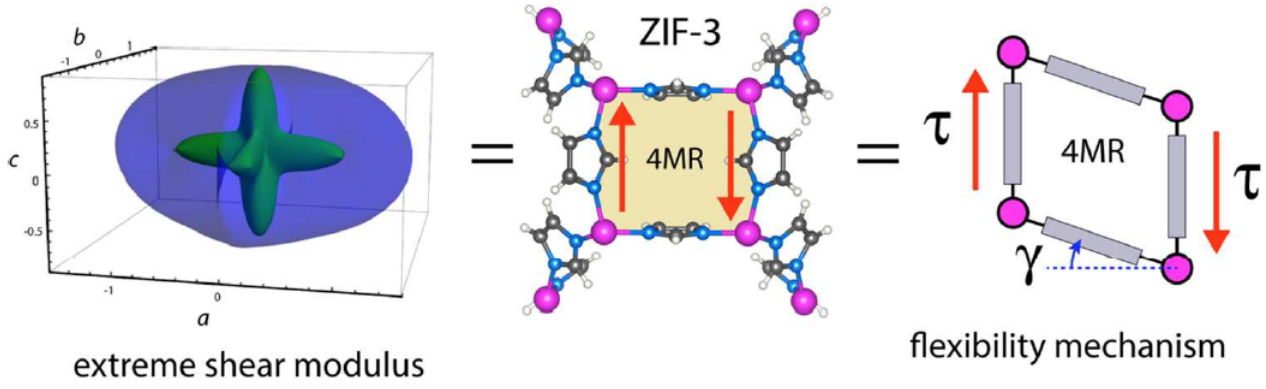

Figure 3.14.1: Shear modulus representation (Left) 3-D surface G(u,v) of ZIF-3, where the maximum and minimum values are represented as blue and green surfaces, respectively. (Middle) Projection down the [110] axis of ZIF-3, highlighting the location of the four-membered ring (4MR). (Right) The accompanying "pivot-and-strut" model further emphasising the pliant 4-node configuration, which is highly susceptible to a shear strain γ (angular distortion) generated by a pair of antiparallel shear stresses τ.

3.15 Hydrogen Dynamics in Condensed Matter: Linking Neutron Data to First-principles Predictions

Felix Fernandez-Alonso (ISIS), Kacper Druzbicki (JINR Dubna, AMU Poznan) and Matthew Krzystyniak (ISIS, Nottingham Trent University)

In the period 01/08/14 to 01/08/15, we continued our research programme, namely using the SCARF cluster in research projects aimed at linking periodic DFT calculations using CASTEP to the interpretation of Compton (NCS) and inelastic (INS) neutron-scattering experiments carried out at the ISIS Pulsed Neutron and Muon Source, Rutherford Appleton Laboratory [1- 8]. Emphasis has been placed on hydrogen-containing materials of fundamental and technological interest. We continued developing software tools in Matlab to process and link the output of modelling packages such as CASTEP and Gaussian 09 and data format converters provided within ACLIMAX program with observables directly measured in neutron spectroscopy. Work published to date includes comparison of model calculations with experimental NCS in lithium hydride (including its deuterated counterpart) [1, 4, 3, 5] and squaric acid [1], and hydrogen dynamics in the prototypical proton conductor caesium hydrogen sulphide [2]. Results of these studies have been presented at *Molecular Spectroscopy User Group Meeting*, (Abingdon, January 2015) [1- 4], *The 4th International Symposium on Energy Challenges and Mechanics - working on small scales* (Aberdeen, August 2015) [4], and the *European Neutron Scattering Conference* (Zaragoza, August 2015) [5]. Brief summaries of the work accomplished to date are enclosed below.

Model Calculations on Lithium Hydride and Deuteride and Squaric Acid: Comparison to NCS Experiments

Theoretical nuclear momentum distributions for solid lithium hydride and lithium deuteride [1-4, 6 -8] as well as squaric acid, an organic antiferroelectric material containing hydrogen, carbon, and oxygen, were performed within the framework of plane-wave density functional theory, followed by the computation of phonon-dispersion relations and vibrational densities of states. The computational results were compared with existing neutron Compton scattering experiment results. Beyond the usual case of the proton, our approach enabled direct access to detailed line shape information associated with the underlying nuclear-momentum distributions of both deuterium and lithium. For oxygen and carbon, mean kinetic energies were obtained directly from the neutron data from squaric acid. From an instrumentation point of view, this work provides a suitable platform for a detailed assessment of existing capabilities and future developments in mass-selective neutron spectroscopy on the VESUVIO spectrometer at ISIS.

Hydrogen Dynamics in a Solid Proton Conductor $CsHSO_4$

SCARF computational resources have been used to calculate momentum distributions in the solid proton conductor caesium hydrogen sulphide $CsHSO_4$ [5-8]. The motivation for this work has been threefold: (i) to investigate how much the investigation of the proton momentum distribution below the superprotonic phase transition, in the crystallographic phase III, can give insight into possible mechanism responsible for the onset of the proton conduction, (ii) to check the hypothesis that proton motions in $CsHSO_4$ are purely classical down to cryogenic temperatures, a task that can be accomplished by comparing measured and calculated proton momentum distributions and

establishing how much of the measured widths of momentum distributions can be explained by classical Maxwell-Boltzmann distribution (iiii) benchmark first-principles computational models. PW-DFT electronic structure and phonon calculations using the CASTEP code within the GGA approximation have been performed for $CsHSO_4$ (Figs. 3.15.1 and 3.15.2) and compared with experimental NCS data. Linear-response phonon calculations were employed to obtain second moments of the nuclear momentum distribution using the methodology established and tested on lithium hydride [1]. Fair agreement with experimental values for the isotropic widths of the proton momentum distribution was achieved. Building upon this experience, we performed ab initio calculations in CASTEP within the generalised-gradient approximation, using both 'standard' and 'hard' formulations of the Perdew-Burke-Ernzerhof functional supplemented by Tkatchenko-Scheffler dispersion corrections. Both approaches provided an excellent description of the known structure, underlying vibrational density of states, and nuclear momentum distributions measured at 10 and 300 K. From this analysis, we found that only the heavier caesium atoms reach the classical limit at room temperature. Contrary to expectation, sulfur exhibited a more pronounced quantum character relative to classical predictions than the lighter oxygen atom. We interpreted this hitherto unexplored nuclear quantum effect as arising from the tighter binding environment of this species.

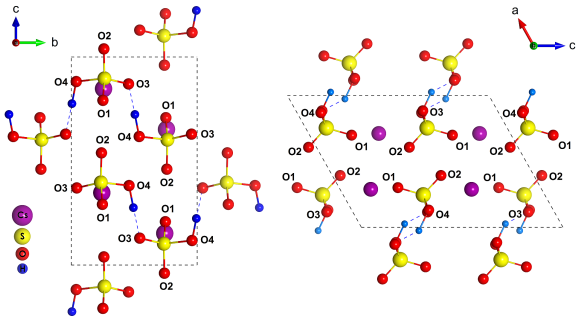

Figure 3.15.1: Structure of CsHSO4 phase III optimised with CASTEP.

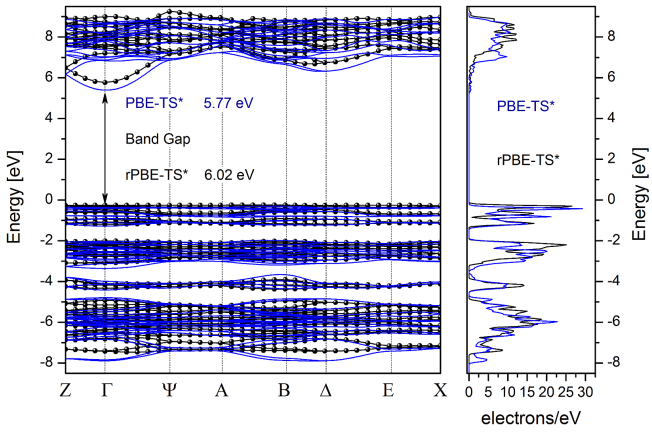

Figure 3.15.2: Electronic band-structure (left) and density-of-states (right) for CsHSO4 phase III calculated with CASTEP.

References

[1] M Krzystyniak, A G Seel, S E Richards, M J Gutmann and F Fernandez-Alonso, 'Mass-selective Neutron Spectroscopy Beyond the Proton', J. Phys. Conference Series, 571, 012002, 2014 [doi:10.1088/1742-6596/571/1/012002]

[2] C Andreani, M Ceriotti, G Chass, C Drechsel-Grau, F Fernandez-Alonso et al., 'Discussion: Nuclear Quantum Dynamics - Protons and Beyond' J. Phys. Conference Series, 571, 012004, 2014 [doi:10.1088/1742-6596/571/1/012004]

[3] M Ceriotti, C Drechsel-Grau, F Fernandez-Alonso, N Greaves, M Krzystyniak et al., 'Discussion: Theoretical Horizons and Calculation', J. Phys. Conference Series, 571, 012013, 2014 [doi:10.1088/1742-6596/571/1/012013]

[4] C Andreani, M Krzystyniak, R Senesi, F Fernandez-Alonso, 'Electron-volt Neutron Spectroscopy: Opportunities in the Study of Nanomaterials For Energy Applications, Book Chapter or Section: In Nanomaterials for Energy Applications. Handbook of Characterization and Properties of Nanostructured Materials edited by C K Loong, 2015.

[5] M. Krzystyniak, K. Druzbicki, and F. Fernandez-Alonso, 'Nuclear Dynamics in the Metastable Phase of the Solid Acid Caesium Hydrogen Sulfate', Physical Chemistry Chemical Physics, 2015, submitted.

[6] M. Krzystyniak and F. Fernandez-Alonso, 'Mass-selective neutron spectroscopy beyond proton', poster presented at the, Molecular Spectroscopy User Meeting, Abingdon, January, 2015

[7] M. Krzystyniak, 'Mass-selective neutron spectroscopy', invited talk presented at the 4th International Symposium on Energy Challenges and Mechanics - working on small scales, August, 2015

[8] M. Krzystyniak, G. Romanelli, and F. Fernandez-Alonso, 'Mass-selective neutron spectroscopy', poster presented at the *6th European Conference on Neutron Scattering ECNS 2015,* August **2015**, Zaragoza, Spain.

3.16 ORAC Broad Band Radiative Flux Retrieval

Matthew Christensen, RAL Space

SCARF is used to run the new broadband flux retrieval called BUGSrad on ORAC (A)ATSR satellite series. Radiative fluxes are retrieved at the 1-km pixel scale resolution of the satellite retrieval first assuming no clouds (clear-sky) and then using the optical property retrievals for cloud and aerosol (observed). These data are then aggregated onto a 1°×1° grid and averaged over JJA for 2008. Data was recently presented at the 14th AeroCom meeting at ESA ESRIN.

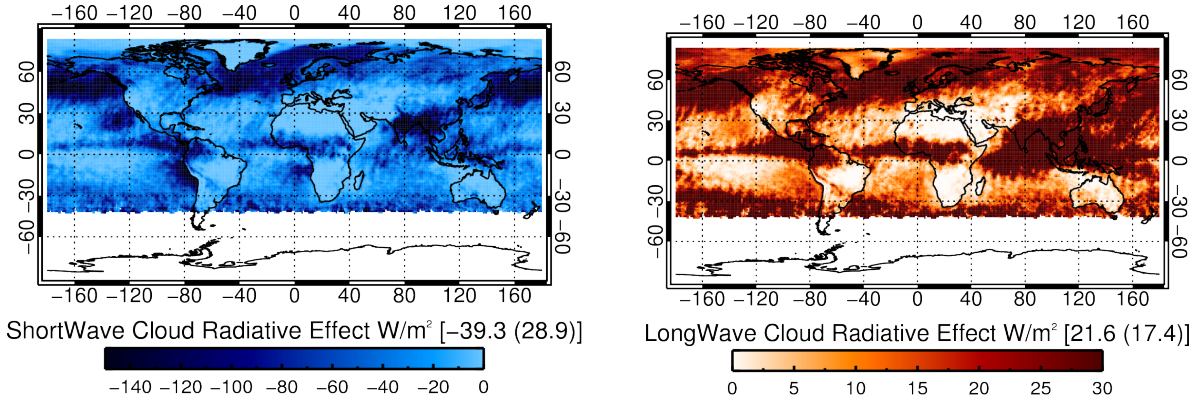

Figure 3.16.1: Cloud radiative effect $CRE = F_{clear} - F_{observed}$, the difference in outgoing top of atmosphere broadband radiation between clear- and all-sky conditions in the long and shortwave (left and right, respectively). Global mean values and standard deviations weighted by latitude are provided in brackets

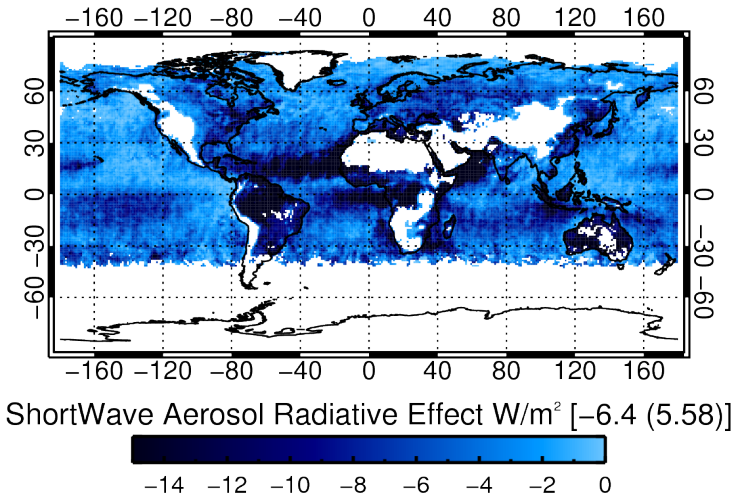

Figure 3.16.2: A first approximation of the aerosol radiative effect.

3.17 Temperature-dependent Vibrational Dynamics and Ferroelectricity in Croconic Acid

Sanghamitra Mukhopadhyay,[1,2] Matthias J. Gutmann,[1] and Felix Fernandez-Alonso[1,3]

[1]*ISIS Facility, Rutherford Appleton Laboratory, Chilton, Didcot, Oxfordshire OX11 0QX*
[2]*Department of Materials, Imperial College London, Exhibition Road, London SW7 2AZ*
[3]*Department of Physics and Astronomy, University College London, London WC1E 6BT*

Organic ferroelectrics are technologically important materials because of their potential use in low-cost organic electronics. Croconic acid ($C_5O_5H_2$, hereafter CA) is an important member of this family of materials, displaying ferroelectricity in its crystalline form at room temperature and beyond. It is thought that the dynamics of the hydrogen bond plays an important role in CA, including the known (and yet-to-be explained) increase in unit-cell polarizability with increasing temperature. Inelastic neutron-scattering (INS) experiments and first-principles calculations as a function of temperature have been performed to address this question.

On the experimental front, we have used TOSCA at ISIS and LAGRANGE at ILL to investigate the temperature dependence of INS spectra for CA over the range T=5-300 K. To interpret the experimental data, we have used state-of-the-art density functional theory (DFT) as implemented in the plane-wave DFT code CASTEP. Norm-conserving pseudopotentials were used with the Perdew-Burke-Ernzerhof (PBE) functional within the generalized-gradient approximation (GGA) with a plane-wave cutoff of 800 eV. These calculations show that dispersion corrections to the PBE functional (PBE+D) are necessary in order to explain the structural and spectroscopic neutron data. Apart from phonon calculations within the quasi-harmonic approximation, molecular dynamics (MD) simulations were also performed on a simulation cell containing 384 atoms. The lattice-dynamics simulations used 128 processors on SCARF, taking more than three weeks to obtain full phonon-dispersion relations across the Brillouin zone. MD simulations required 500 processors and 10 days per picosecond. Given these timescales, additional computing power on SCARF would be most welcome to speed up these simulations.

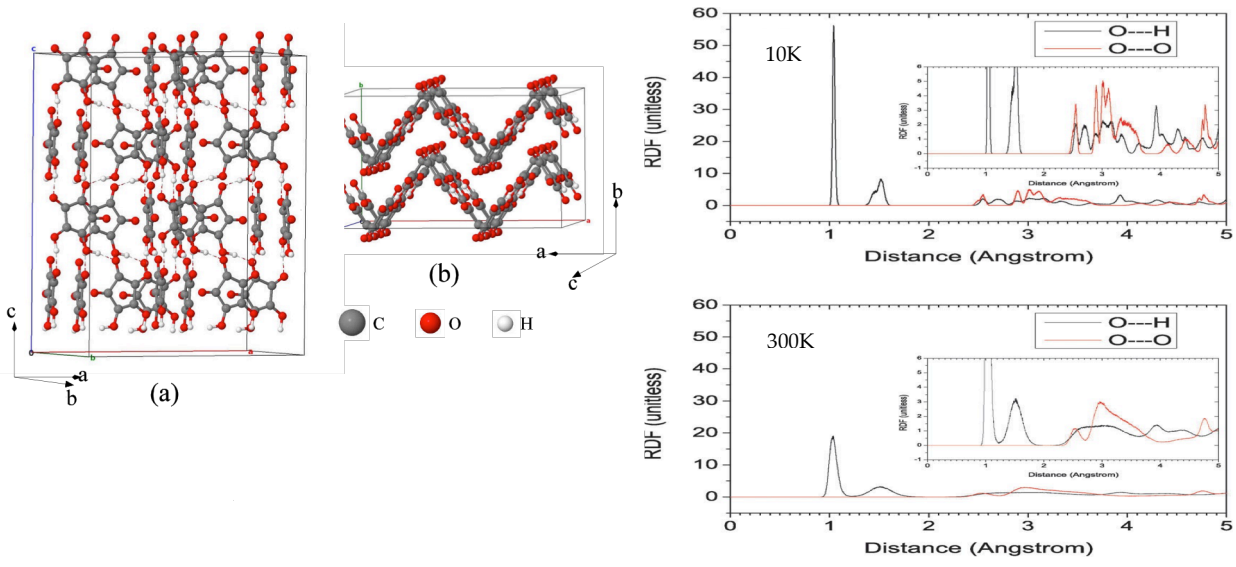

Figure 3.17.1: Left: MD simulation box containing 384 atoms. Middle: side view of two layers of crystalline CA. Right: radial distribution functions of CA at 10K and 300K, obtained from the MD simulations up to 10 picoseconds.

From the analysis of the MD simulations, we find that the medium-range order associated with O-H and O-O correlations are affected by increasing temperature without any change in the characteristic long-range layered structure of the material. Further analysis reveals that the presence of a soft phonon mode associated with the out-of-plane motion of the hydrogen ion in the hinge position of the layered structure of CA plays correlates with the temperature dependence of the ferroelectric response. The calculated temperature-dependent polarisation using the Berry-phase method compares well with experimental data.

3.18 Vibrational Dynamics of Carbon Tetrachloride from Inelastic Neutron Scattering and Density-functional Theory

Oriol Abril Pla,[1] Daniel Moreno García,[1] Sanghamitra Mukhopadhyay,[2,3] Luis Carlos Pardo,[1] Josep Lluís Tamarit,[1] and Felix Fernandez-Alonso[2,4]

[1]*Grup de Caracterització de Materials, Departament de Física i Enginyeria Nuclear, Universitat Politècnica de Catalunya*
[2]*ISIS Facility, Rutherford Appleton Laboratory, Chilton, Didcot, Oxfordshire OX11 0QX*
[3]*Department of Materials, Imperial College London, Exhibition Road, London SW7 2AZ*
[4]*Department of Physics and Astronomy, University College London, London WC1E 6BT*

Carbon tetrachloride (CCl_4), a clear, colourless, and volatile liquid with a characteristic sweet odour is widely used as a cleaning agent, as a precursor to refrigerants, and in fire extinguishers. It is also responsible for the depletion of the ozone layer and for global warming. CCl_4 is composed of four chlorine atoms positioned symmetrically as corners in a tetrahedral configuration joined to a central carbon atom by single covalent bonds. An atomistic understanding of this material is of relevance to understand its adverse effect on the environment.

Inelastic neutron scattering (INS) experiments were performed on solid CCl_4 at low temperature using the TOSCA spectrometer at ISIS. To interpret the INS data, first-principles simulations were performed using the plane-wave DFT code CASTEP. As a first step in this study, linear-response theory was used to calculate vibrational frequencies. A comparison of these computational results for an isolated CCl_4 molecule is shown in Fig. 3.18.1.

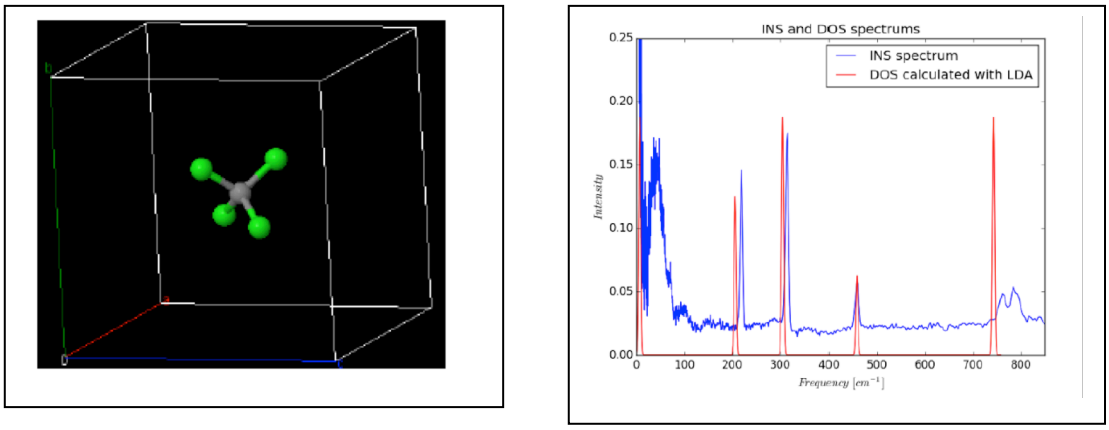

Figure 3.18.1: Left: structure of an isolated CCl_4 molecule. Right: vibrational density of states compared to INS data.

Analysis of the vibrational frequencies reveal that the vibrational modes above 700 cm^{-1} correspond to the asymmetric stretch of C-Cl bonds, the vibration around 440 cm^{-1} is the symmetric stretch of C-Cl bonds, followed by Cl-C-Cl bending and twist modes involving or excluding the central carbon atom at 300 cm^{-1} and 200 cm^{-1}, respectively.

The agreement with experimental data is quite satisfactory, although we note a couple of important discrepancies, namely, the doublet structure observed above 700 cm^{-1} and a prominent and broad low-energy mode below 100 cm^{-1}. Solid-state calculations are in progress to identify the microscopic origin of these additional features.

3.19 Effect of lattice structure on fast electron transport within dual layer targets

R. J. Dance, N. M. H. Butler, R. J. Gray, D. A. Maclellan, H. Xu and P. McKenna, Department of Physics, SUPA, University of Strathclyde, Glasgow, G4 0NG, UK

D. R. Rusby, G. G. Scott, A. P. L. Robinson, D. Neely Central laser Facility, STFC Rutherford Appleton Laboratory, Oxfordshire, OX11 0QX, UK

M. P. Desjarlais Sandia National Laboratories, PO Box 5800, Albuquerque, NM 87185, USA

B. Zielbauer, V. Bagnoud PHELIX Group, GSI Hemholtzzentrum fuer Schwerionenforschung GmbH, D64291 Darmstadt, Germany

The transport of fast electrons in solid density materials attracts a great deal of research interest due to its wide ranging from fast ignition fusion [1, 2], to the generation of intense x-ray and ion sources [3], and production of warm dense matter states with astrophysical relevance [4]. In many of these a smooth, collimated fast electron beam profile is favourable. The interaction of a 10^{20} Wcm^{-2} laser with a solid target produces a large current (mega Ampere scale) of relativistic electrons. It has been shown recently that the electrical resistivity and lattice structure of the solid through which an electron beam propagates, plays a pivotal role in the resulting fast electron beam profile [5–7]. A filamented profile of the electron beam is particularly damaging to the transport of electrons and their energy.

Many measurements of the transport physics in the target, particularly those utilising x-ray measurements, rely on a buried layer within the target [8, 9] and as such, understanding the effect of the boundary between layer and target bulk on the transport, is important [10].

To investigate the effect of lattice structure and low temperature electrical resistivity on the underlying electron transport physics numerically, a 3D hybrid-PIC code [11] on the SCARF cluster is used to simulate the transport of fast electrons within layered carbon targets. The grid used for all the simulations and is 400 μm × 400 μm×200μm,with cell size equal to $\Delta X=\Delta Y=\Delta Z$ = 1μm, sampled every 200 fs. A total of 2×10^8 macro- particles are injected over a 725 fs pulse duration. The peak intensity modelled is ~ 1×10^{21} W/cm^2. Figure 1 shows simulations of 200 μm layered targets consisting of vitreous carbon (VC) in thicknesses of 10 μm, 100 μm and 190 μm at the front surface, and the remaining thickness is diamond (D). For each, fast electron density ($\log_{10}m^{-3}$), magnetic field (T) and electrical resistivity (Ωm) are shown from top row to bottom respectively. These images show an increase in beam filamentation as the front surface of VC increases in thickness.

This investigation primarily shows that there is a minimum propagation distance of ~60 μm of vitreous material, required to facilitate sufficient growth of resistive magnetic fields that drive resistive filamentation of the fast electron beam. The presence of disordered lattice structure material in the target produces strong fila- mentation, independent of its location within a double-layered target, when the thickness ≥ 60 μm. The effect of the boundary is also seen to be far less than for these targets where ΔZ across the boundary is high. Publication of these results and further work in Dance et al. [12].

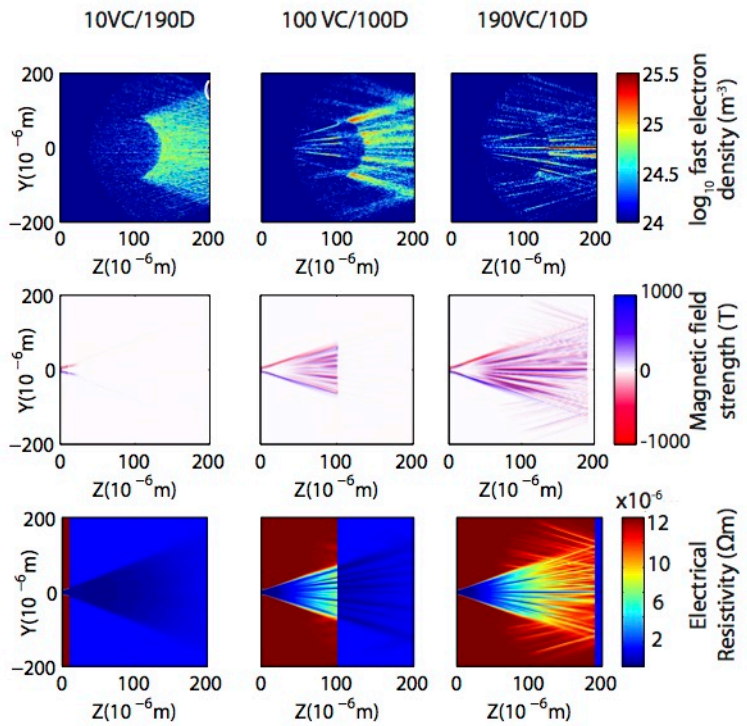

Figure 3.19.1: Simulations of layered targets consisting of 10 μm Vitreous Carbon (VC) and 190 μm Diamond (D) (left column), 100 μm VC and 100 μm D, and 190 μm VC and 10 μm (right column). In each the top image is fast electron density (log10 m−3), centre image is z- component of magnetic field (T) and bottom image the electrical resistivity (Ωm).

Acknowledgements

The authors would like to thank the CLF for their continuing support, in particular Dr Alex Robinson for support and use of the Zephyros code. We gratefully acknowledge the use of computing resources provided by STFC's e-Science project. This work is financially supported by EPSRC (grant numbers EP/J003832/1 and EP/K022415/1) and STFC (grant number ST/K502340/1). The research leading to these results is sponsored by the Air Force Office of Scientific Research, Air Force Material Command, USAF, under grant number FA8655-13-1-3008.

References

[1] M. Tabak et al, Phys. Plasmas 1, 1626 (1994)
[2] M. Roth et al, Phys. Rev. Lett. 86, 436-439 (2001)
[3] A. Macchi et al, Rev. Mod. Phys. 85, 751 (2013)
[4] A. Benuzzi-Mounaix et al, Phys. Scr. T161, 014060 (2014)
[5] D.A. Maclellan et al, Phys. Rev. Lett 111, 095001 (2013)
[6] D.A. Maclellan et al, Phys. Rev. Lett 113, 185001 (2014)
[7] P. McKenna et al, Phys. Rev. Lett 106, 185004 (2011)
[8] J. A. Koch et al., Laser Part. Beams 16, 225 (1998)
[9] K.L.Lancaster et al.,Phys.Rev.Lett.80,045401(R)(2009)
[10] X. Yang et al., Eur. Phys. D 68, 30 (2014)
[11] A.P.L.Robinsonetal.,Phys.Rev.Lett.,108,125004(2012)
[12] R. Dance et al., Plasma Phys. Cont. Fusion (at press)

3.20 Simulation of fast electron transport for fast ignition relevant parameters

R. J. Dance, N. M. H. Butler, D. A. Maclellan, R. J. Gray and P. McKenna , Department of Physics, SUPA, University of Strathclyde, Glasgow, G4 0NG, UK

M. P. Desjarlais, Sandia National Laboratories, PO Box 5800, Albuquerque, NM 87185, USA

A. P. L. Robinson, D. Neely, Central Laser Facility, STFC Rutherford Appleton Laboratory, Oxfordshire, OX11 0QX, UK

The ability to control the transport of laser-generated fast electrons within solid density targets has numerous important applications. One of the most well known of these is the fast ignition (FI) approach to inertial confinement fusion, in which a high current electron beam acts as the ignitor for a hydrogenic fuel pellet [1]. In the scheme outlined in Figure 3.20.1 (a), a re-entrant cone is used to place the electron source closer to the compressed region of the DT fuel. It has been shown that for ignition of the fuel to occur, that annular fast electron beam profile is favourable due to the increase of electron current that can propagate [2].

In recent work, annular fast electron patterns have been observed both experimentally and numerically for a silicon target [3–6], which is attributed to the effects of the target resistivity and lattice structure. In this work we numerically investigate the effect of low temperature (below the Spitzer regime) resistivity profile on the resulting electron transport. Figure 3.20.1 shows the re-entrant cone geometry, usually made from gold, with a silicon insert applied to the re-entrant cone. Simulations on the SCARF cluster, not only enables the simulation of the experimental conditions obtained at facilities such as the Vulcan facility at Rutherford Appleton laboratory (such as those in [3, 4]), but further the scaling up to fast ignition conditions for inertial confinement fusion [8]. Simulation of complex and novel target geometries is also possible before extensive laboratory testing.

Electrons generated in these interactions are also rapidly accelerated to high velocities, and in very high numbers, therefore diagnosis of small scale beam structure is computationally intense. To make the calculations such as this tractable, a 3D hybrid PIC code [7] is used on the SCARF cluster, to model a grid of 400 μm × 400 μm × 400 μm, containing a total of 2×10^8 macroparticles, and cell size $\Delta X = \Delta Y = \Delta Z = 1$ μm. By assuming a laser to fast electron energy conversion efficiency $\eta = 30\%$, with a laser pulse duration of 725 fs (wavelength of 1 μm) a resulting peak intensity of $\sim 1 \times 10^{21}\mathrm{W/cm^2}$ is modelled.

By simulation, we were able to show the occurrence of annular transport in silicon targets on a scale directly relevant to fast ignition scale experiments. The application of this into a re-entrant cone geometry for FI and subsequent simulations such as shown here, resulted in publication in early 2015 (P. McKenna et al.) [8] as a possible path for future fast ignition fusion experiments.

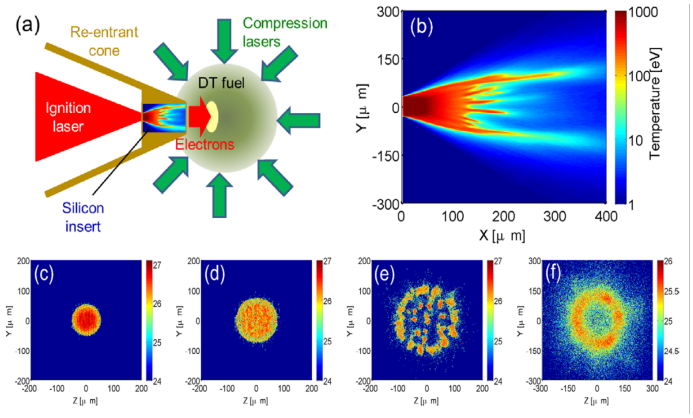

Figure 3.20.1: From reference [8] (a) Schematic illustrating a cone fast ignition scheme with a silicon insert to induce an annular fast electron beam transport pattern (b) Background target temperature in the [X-Y] mid-plane for L=400 μm case (c-f) Log10 fast electron density maps (m−3) at the rear surface [Y-Z] plane for (c) L = 50 μm, (d)L=100μm,(e)L=200μmand(f)L=400μm case.

Acknowledgements

The authors would like to thank the CLF for their continuing support, in particular Dr Alex Robinson for support and use of the Zephyros code. We gratefully acknowledge the use of computing resources provided by STFC's e-Science project. This work is financially supported by EPSRC (grant numbers

EP/J003832/1 and EP/K022415/1) and STFC (grant number ST/K502340/1). The research leading to these results is sponsored by the Air Force Office of Scientific Research, Air Force Material Command, USAF, under grant number FA8655-13-1-3008.

References

[1] M. Tabak et al., Phys. Plasmas 1, 1626 (1994)

[2] J. R. Davies et al., Phys. Rev. E 69 (2004)

[3] D.A. Maclellan et al., Phys. Rev. Lett 111, 095001 (2013)

[4] D.A. Maclellan et al., Phys. Rev. Lett 113, 185001 (2014)

[5] P. McKenna et al., Phys. Rev. Lett 106, 185004 (2011)

[6] D.A. Maclellan et al., Laser Part. Beams 31, 475 (2013)

[7] A. P. L. Robinson et al., Phys. Rev. Lett., 108, 125004 (2012)

[8] P. McKenna et al., Plasma Phys. Cont. Fusion 57, 064001 (2015)

3.21 Solubility of simple gases in organic solvents using molecular dynamics simulations.

C. W. Yong, W. Smith and I. T. Todorov, Computational Chemistry Group, SCD, Daresbury Laboratory.

J. Satherley, Department of Chemistry, University of Liverpool, Liverpool L69 7ZD.

Gas composition in solution is a crucial parameter affecting catalyst performance. The solubility of a gas in a liquid is a fundamental physical property of a system and of interest both to the chemist and chemical engineer. In gas-liquid homogenous catalytic reactions the solubility of gases is a crucial parameter in the process. For instance, since the reaction occurs in the liquid phase, the reaction kinetics and the reactor design are highly dependent on gas solubilities. However, gas solubilities can be influenced by many factors such as temperature, pressure, and even the relative compositions of solvent mixtures. A detailed understanding of how these factors control the solubility of a gas is crucial as there is always an economic incentive to control or maximise the gas solubility in a given liquid composition.

In this project we intend to investigate via molecular dynamics (MD) simulation studies the temperature dependence of CO solubility in methanol (MeOH)/methyl propanoate (MPRO) mixtures, an important industrial process for the manufacturing of thermoplastic materials. Such study is important to provide structural insight at an atomistic detail how small gas molecules are stabilised in organic solvents, and from such an optimum solvent component mixture may be identified that improves the solubility of the gas molecules. This is also an important insight for other manufacturing industry involving organic solvents.

In this on-going project, we used DL_FIELD to set up the simulation model using CHARMM force field. DL_POLY_4 was used to run the MD simulation in Scarf. The model consists of CO with a mole fraction of ~5 x 10^{-3} in a MeOH/MPRO solvent mixture.

Our preliminary analysis indicates that the CO gas molecule is stabilised in a hydrophobic cage, with the ethyl groups of the MPRO molecules are the major component that made up the hydrophobic cavity wall. The cavity is in turn stabilised by the formation of a series of hydrogen bond network in such a way that the hydrophobic alkyl groups of the solvent molecules are orientated towards one another to provide maximum hydrophobic contacts.

Diagram below identifies one such cavity with the CO molecule highlights in pink. We intend to carry out further simulations and analysis in order to characterise the structural and dynamic behaviour of these cavities.

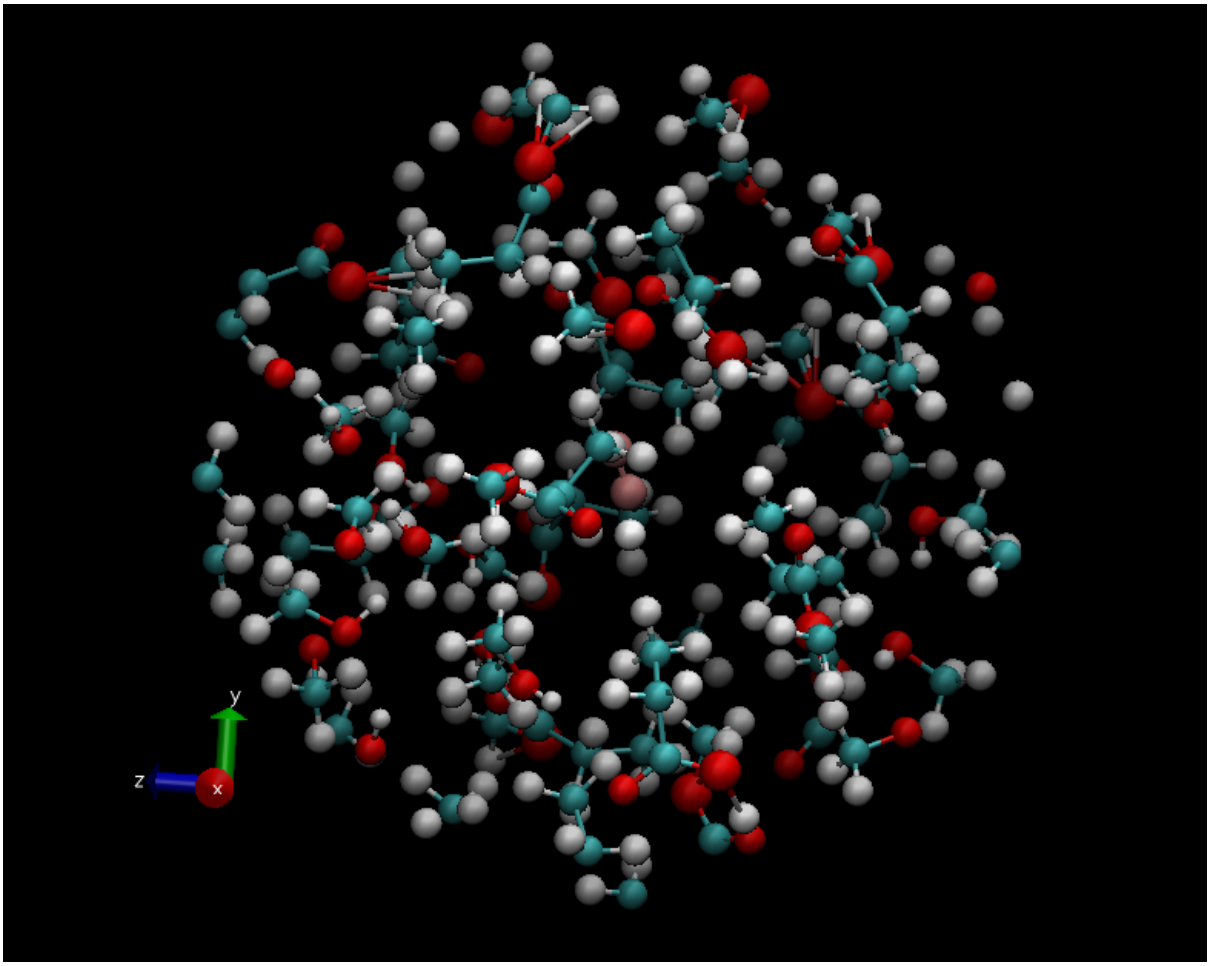
y
z
x

3.22 Neutron tomography simulations of IMAT instrument using SCARF

G. Burca (ISIS), W. Kockelmann (ISIS), A. Sajid (STFC), D. Ross (STFC)

The new instrument IMAT [1] at ISIS TS-II is the first facility developed on a pulsed source combining cold-neutron radiography and diffraction for materials and engineering sciences. A straight square neutron guide (~44 m) transporting the neutrons from the moderator to the sample is required to combine imaging and diffraction modes and to achieve a good energy-resolution and energy-dependent radiography.

After a detailed investigation of the IMAT instrument geometry and optimization of the instrument parameters using Monte Carlo techniques by taking into account both capabilities of the instrument [2] simulated imaging data have been acquired by using a parallelised version of McStas 2.0 software package on SCARF-RAL cluster. These simulations allow the study of energy-dependent attenuation effects as well as effects of spectral inhomogeneities on white-beam tomographies for which attenuation coefficients are averaged over a broad energy band.

Of a particular relevance for an instrument on a pulsed source such as IMAT is that it facilitates the collection of data with variable neutron bandwidths and time-resolved, for either white-beam imaging or selection of narrow wavelength bands so that the energy-dependent attenuation effects can be studied and corrected. Moreover, a diffraction/imaging oriented sample Sample_nxs.comp [3] where his structure defined by means of the NXS crystallography library for neutron cross section calculations [4] was uploaded on McStas 2.0 from SCARF and used in the IMAT tomography instrument setup.

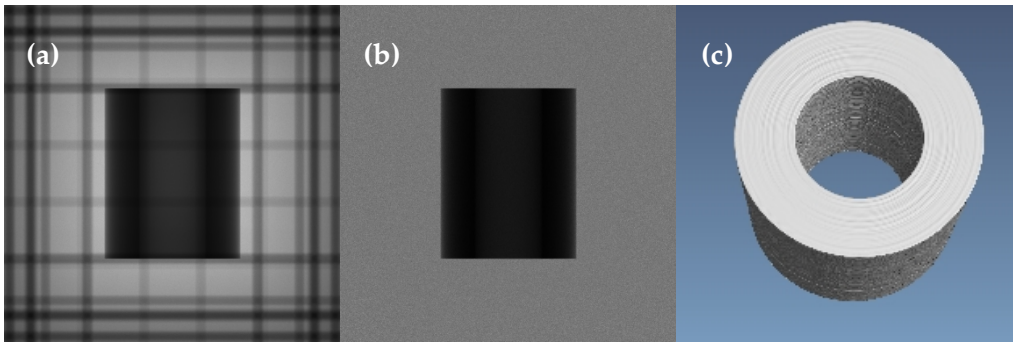

Figure 3.22.1: Simulated data of cylinder of 10 cm height with L/D=2000 and white beam spectrum. (a) Radiography obtained with SCARF. (b) Radiography after flat field correction. (c) 3D volume rendered tomography.

References

[1] Kockelmann, W., Burca, G. et al., *Status of the Neutron Imaging and Diffraction Instrument IMAT*, Physics Procedia 69 (2015) 71-78

[2] G. Burca, W. Kockelmann, J.A. James, M.E. Fitzpatrick, *Modelling of an imaging beamline at the ISIS pulsed neutron source*, Journal of Instrumentation, 8 (2013), P10001

[3] M. Boin, *nxs: a program library for neutron cross section*, J. Appl. Cryst. 45 (2012) 603

[4] https://bitbucket.org/mirkoboin/nxs

3.23 Phonon Excitations in single to – triple L-Alanine using Density Functional Simulations and Diffuse Scattering

Sanghamitra Mukhopadhyay and Matthias J. Gutmann, ISIS Facility, Rutherford Appleton Laboratory

Amino acids are the building blocks of proteins present in all living organisms. These acids form molecular crystals largely stabilized by electrostatic interactions. A little investigation exists on these molecular crystals, particularly on lattice dynamical properties, however, it would be desirable to know both the structure and dynamics to understand their behaviour. Determination of the lattice dynamics of these systems is also important to reveal important insights into the different types of bonding mechanisms, from covalent bonding to hydrogen bonding to van-der Waals interactions, responsible for molecular crystal formation.

Alanine ($C_3H_7NO_2$) is the smallest naturally occurring chiral amino acid. L-Alanine crystallizes in the orthorhombic $P2_12_12_1$ space group with four (^+H_3N-C_2H_4-CO_2^-) zwitterionic molecules in the unit cell (see Fig. 3.23.1. (Left)). These molecules are joined by three networks of hydrogen bonds of unequal strength with pairs of layers anti-parallel to one another. Each layer is stabilized by characteristic head-to-tail hydrogen bonds with all three available protons of the ammonium group ($NH3^+$) forming a single N-H···O hydrogen bonds with oxygen atoms of three carboxylate groups (CO^{2-}) of the nearest amino acid molecules. This structural arrangement gives rise to an ionic solid with strong intermolecular interactions with an anharmonic potential. In addition, the L-alanine crystals are similar to infinite parallel b-sheets found in proteins.

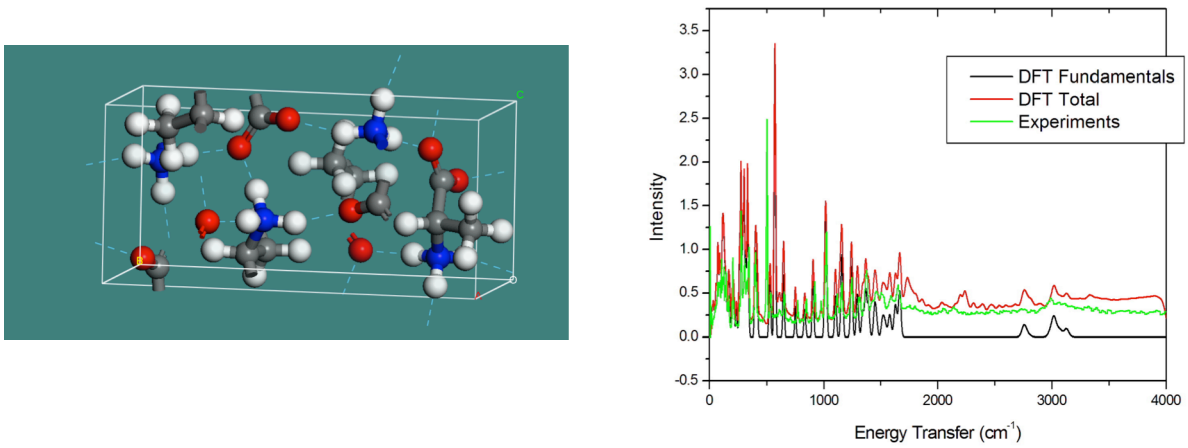

Figure 3.23.1: L-Alanine unit cell (left) and the inelastic neutron spectrum (right) obtained from DFT simulations are shown together with the experiments.

We investigated structures of L- and double-L alanine using CASTEP code and Perdew-Burke-Ernerhof generalised gradient approximation (PBE-GGA) and also dispersion corrected PBE (PBE+D) in DFT. The experimentally obtained structures were relaxed using BFGS method. The calculated bond lengths were in agreement with neutron diffraction results within 3%. The lattice dynamical calculations have been done using density functional perturbation theory (DFPT) within the DFT as available in the CASTEP code. The calculated vibrational spectrum compared well with

experimental spectrum obtained from TOSCA instrument at ISIS (see Fig. 3.23.1. Right). All calculations have been done on SCARF computers.

Comparing the calculated results with experiments, we find that dispersion correction in PBE is required to explain the van-der Walls interactions present between the layers of the crystalline structure of alanine. Motion of three different kinds of hydrogen bonds have been identified in the 500-600 cm^{-1} region of the INS spectrum. Born effective charge tensor are analysed to understand the bonding nature of these three different solid state phase alanines.

References:

[1] A. R. Kolatkar, J. B. Clarage, and G. N. Phillips, Acta Cryst. D50, 210-218 (1994).
[2] P. R. Tulip and S. J. Clark, Phys. Rev. B, **74**, 064301 (2006).
[3] M.J. Gutmann, G. Graziano, S. Mukhopadhyay, K. Refson, M. von Zimmermann, "*Computation of diffuse scattering arising from one-phonon excitations in a neutron time-of-flight single-crystal Laue diffraction experiment*", J. App. Cryst. **48**, 1122-1129 (2015).

3.24 Single Ion Motion in Molten Salt

Sanghamitra Mukhopadhyay and Franz Demmel, ISIS Facility, Rutherford Appleton Laboratory,

Molten salts are technologically important materials because of their unique properties of high heat capacity, low vapour pressure and high electrical conductivity. The large heat capacities of molten salts make them attractive as heat transport media, as e.g. for heat storage in modern solar power plants or as coolant in next generation nuclear reactors. Recently molten salts are also used as the dielectric medium in high-temperature fuel cells.

These salts are fluids with particles carry electric charges. The interaction is given by the slow decaying Coulomb interaction which is responsible for some of their peculiar features. The molten alkali halides are the simplest class of molten salts with only a single cataion and an anion. Such simplicity initiated a lot of interest from computational and experimental side.

Inelastic X-ray scattering experiments on molten alkali halides have demonstrated acoustic- and optic-type modes. Recently single particle dynamics on a microscopic level have been investigated using quasi-elastic neutron scattering (QENS) experiments. To interpret these results, ab-initio molecular dynamics (MD) simulations using density functional theory (DFT) as implemented in CASTEP code has been performed on SCARF computer. A simulation cell size of 512 atoms has been melted using NVT ensemble with norm-conserving pseudopotentials and the Perdew-Burke-Ernzerhof (PBE) functional within the generalized-gradient approximation (GGA) with a plane-wave cut off of 1000 eV. The supercell of a 512 atom molten NaF supercell is shown in Fig. 3.24.1.

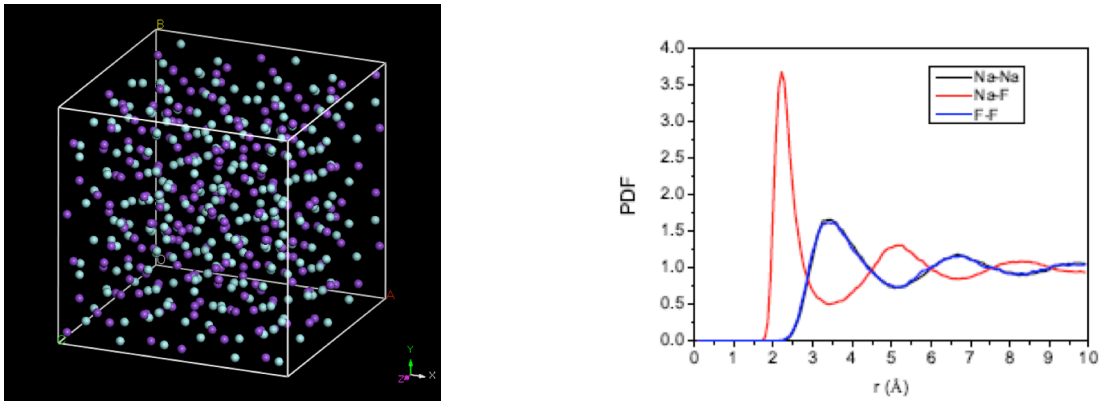

Figure 3.24.1: (left) 512 atom supercell of molten NaF (right) Radial distribution function of atomic distances of molten NaF.

From the 512 atoms molten salt simulation cell a 64 atom cell has been cut out and production run has been carried out for 60 ps using NVE ensemble. Calculated neutron observables particularly shape and intensity of $S(Q,\omega)$ compares well with experiments. Analysis of the quasi elastic neutron spectrum shows that the motion of Na and F in the molten salt is highly correlated at least upto 0.1ps. Diffusion coefficients of these species are calculated and the Na diffusion constant compares well with published results.

4 APPENDIX: SCARF HARDWARE DETAILS

Host group	CPU type and frequency	Nodes	Cores /node	Total cores	Interconnect	Total memory
SCARF15	Intel E5-2650v3 @ 2.30GHz	68	20	1360	FDR Infiniband	8704 GB
SCARF14	Intel E5-2650v2 @ 2.60GHz	56	16	896	QDR Infiniband	7168 GB
SCARF13	Intel E5-2660 @ 2.20GHz	68	16	1088	QDR Infiniband	4352 GB
SCARF12	Intel X5675 @ 3.06GHz	20	12	240	QDR Infiniband	960 GB
SCARF11	Intel X5660 @ 2.8GHz	32	12	384	QDR Infiniband	768 GB
Lexicon-2/ SCARF10	Intel E5530 @ 2.40GHz	104	8	832	DDR Infiniband	2496 GB
IBIS/ SCARF09	Intel E5462 @ 2.80GHz	48	8	384	SDR Infiniband	768 GB
Lexicon 1 (2013)	Intel E5-2660 @ 2.20GHz	16	16	256	GB Ethernet	1024 GB
Grand Totals		**412**		**5440**		**26240 GB**

5 APPENDIX: INDEX OF FIGURES

6 APPENDIX: PUBLICATIONS AND PRESENTATIONS

6.1 Publications

	Title	Authors	Journal
1	Structure and spectroscopy of CuH prepared via borohydride reduction	E.L. Bennett, T. Wilson, P.J. Murphy, K. Refson, A.C. Hannon, S. Imberti,S.K. Callear, G.A. Chass and S.F. Parker	Acta Crystallographica B, accepted for publication. [doi: 10.1107/S2052520615015176]
2	"Soft phonons and fast continuum scattering in $CH_3NH_3PbBr_3$"	I.P. Swainson, C. Stock, S.F. Parker, L. Van Eijck, M. Russina and J.W. Taylor	Physical Review B, 92 (2015) 100303(R).
3	"Structural and spectroscopic characterisation of C4 oxygenates relevant to structure/activity relationships of the hydrogenation of a,b-unsaturated carbonyls"	S.F. Parker, I.P. Silverwood, N.G. Hamilton and D. Lennon	Spectrochimica Acta A: Molecular and Biomolecular Spectroscopy, 153 (2016) 289–297. [doi: 10.1016/j.saa.2015.08.034]
4	"Assignment of the internal vibrational modes of C_{70} by inelastic neutron scattering spectroscopy and periodic-DFT"	K. Refson and S.F. Parker	ChemistryOpen, (2015).[doi: 10.1002/open.201500069]
5	"Direct spectroscopic evidence of the mechanism behind the phase transition of [2,2]-paracyclophane	H. Wolf, N. Lock, S.F. Parker and D. Stalke	Chemistry - a European Journal 21 (2015) 4556–4560 [doi: 10.1002/chem.201405948]
6	"How the surface structure determines the properties of CuH"	E. Bennett, T. Wilson, P.J. Murphy, K. Refson, A.C. Hannon, S. Imberti, S.K. Callear, G.A. Chass and S.F. Parker	Inorganic Chemistry, 54 (2015) 2213-2220 [doi: 10.1021/ic5027009] .
7	"Short-range structure and phonon assignment of the brownmillerite-type oxide $Ba_2In_2O_5$ and its hydrated proton-conducting form $BaInO_3H$"	J. Bielecki, S.F. Parker, D. Ekanayake, L. Börjesson and M. Karlsson	Journal of Materials Chemistry A,2 (2014) 16915-16924. [doi: 10.1039/C4TA03213F].
8	"Tuning Ti-Cr-V-Mo alloys for optimising hydrogen storage in pressurised tanks"	S.K. Callear, A.J. Ramirez-Cuesta, K. Kamazawa S.-I. Towata, T. Noritake, S.F. Parker, M.O. Jones, J. Sugiyama, M. Ishikiriyama and W.I.F. David	Physical Chemistry Chemical Physics, 16 (2014) 16563 - 16572. [doi: 10.1039/c4cp01666a]
9	"IINS study of the molecular properties of pure hydrogen	P.W. Albers, J. Glenneberg, K. Refson and S.F. Parker	Journal of Chemical Physics 140 (2014) 16450. [doi:

	peroxide and its water mixtures of different concentration"		10.1063/1.4871742]
10	"Characterisation of the hydrides in Stryker's reagent: $[HCu\{P(C_6H_5)_3\}]_6$"	E.L. Bennett, P.J. Murphy, S. Imberti and S.F. Parker	Inorganic Chemistry 53 (2014) 2963–2967. [doi: 10.1021/ic402736t]
11	Simulation of density measurements in plasma wakefields using photon acceleration	M. F. Kasim, N. Ratan, L. Ceurvorst, J. Sadler, P. N. Burrows, R. Trines, J. Holloway, M. Wing, R. Bingham, P. Norreys	Phys. Rev. ST Accel. Beams 18, 032801 (March, 2015).
12	Quantitative single shot and spatially resolved plasma wakefield diagnostics	M. F. Kasim, J. Holloway, L. Ceurvorst, M. C. Levy, N. Ratan, J. Sadler, R. Bingham, P. N. Burrows, R. Trines, M. Wing, P. A. Norreys	Phys. Rev. ST Accel. Beams, 18, 081302 (August, 2015).
13	Time-dependent density-functional theory description of exciton binding in alkali halide crystals: The role of Hartree-Fock exchange	R. Webster, L. Bernasconi and N. M. Harrison,	J. Chem. Phys. 142, 214705 (2015).
14	Chaotic Soliton Dynamics in Photoexcited trans Polyacetylene	L. Bernasconi	J. Phys. Chem. Lett. 6, 908 (2015).
15	The hydration structure of formic acid and acetic acid	S. Soffientini, L. Bernasconi and S. Imberti	J. Mol. Liq. 205, 85 (2015).
16	Synthesis and water behaviour of the aqua-soluble dimeric complex [RuClCp(PTA)2-CN:CN-RuClCp(PTA)2] (CF3SO3)(PTA = 1,3,5-triaza-7-phosphaadamantane)	N. Jagadayeva, S. Imberti, L. Bernasconi, M. Serrano-Ruiz, F. Scalambra and A. Romerosa	Chem. Comm. 50, 11587 (2014).
17	Two-dimensional Cs-vacancy superstructure in iron-based superconductor Cs0.8Fe1.6Se2	D. G. Porter, E. Cemal, D. J. Voneshen, K. Refson, M. J. Gutmann, A. Bombardi, A. T. Boothroyd, A. Krzton-Maziopa, E. Pomjakushina, K. Conder, and J. P. Goff	Phys. Rev. B 91, 144114 http://dx.doi.org/10.1103/PhysRevB.91.144114
18	"Monte carlo simulations of the TOSCA spectrometer: Assessment of current performance and future upgrades	R. S. Pinna, S. Rudic, S. Parker, G. Gorini, F. Fernandez-Alonso	EPJ Web of Conferences, 83(03013), 1-5, 2015.

19	Control of wire heating with resistively guided fast electrons through an inverse conical taper	A.P.L.Robinson, H.Schmitz, J.S.Green, C.P.Ridgers, N.Booth, and J.Pasley	Phys. Plasmas, 22, 043118 (2015)
20	Guiding of laser-generated fast electrons by exploiting the resistivity-gradients around a conical guide element	A.P.L.Robinson, H.Schmitz, J.S.Green, C.P.Ridgers, N.Booth	Plasma Phys.Control. Fusion, 57, 064004 (2015)
21	Micromechanical Behavior of Polycrystalline Metal-Organic Framework Thin Films Synthesized by Electrochemical Reaction	I. Buchan, M. R. Ryder, and J. C. Tan	Crystal Growth & Design, 15(4), pp 1991-1999 (2015)
22	Explaining the Mechanical Mechanisms of Zeolitic Metal-Organic Frameworks: Revealing Auxeticity and Anomalous Elasticity	M. R. Ryder and J. C. Tan	Dalton Trans., Themed issue: Flexibility and Disorder in MOFs. Article In Press
23	Mass-selective Neutron Spectroscopy Beyond the Proton'	M Krzystyniak, A G Seel, S E Richards, M J Gutmann and F Fernandez-Alonso	J. Phys. Conference Series, 571, 012002, 2014 [doi:10.1088/1742-6596/571/1/012002]
24	Discussion: Nuclear Quantum Dynamics - Protons and Beyond	C Andreani, M Ceriotti, G Chass, C Drechsel-Grau, F Fernandez-Alonso et al.	J. Phys. Conference Series, 571, 012004, 2014 [doi:10.1088/1742-6596/571/1/012004]
25	Discussion: Theoretical Horizons and Calculation	M Ceriotti, C Drechsel-Grau, F Fernandez-Alonso, N Greaves, M Krzystyniak et al.	J. Phys. Conference Series, 571, 012013, 2014 [doi:10.1088/1742-6596/571/1/012013]
26	Electron-volt Neutron Spectroscopy: Opportunities in the Study of Nanomaterials For Energy Applications	C Andreani, M Krzystyniak, R Senesi, F Fernandez-Alonso	Handbook of Characterization and Properties of Nanostructured Materials edited by C K Loong, 2015
27	Nuclear Dynamics in the Metastable Phase of the Solid Acid Caesium Hydrogen Sulfate	M. Krzystyniak, K. Druzbicki, and F. Fernandez-Alonso	Physical Chemistry Chemical Physics, 2015, submitted
28	Hydrogen-bond Structure and Anharmonicity in Croconic Acid	S. Mukhopadhyay, M. J. Gutmann, and F. Fernandez-Alonso	Phys. Chem. Chem. Phys. 16, 26234 (2014).
29	Temperature Dependent Vibrational Properties and Ferroelectricity of Croconic	S. Mukhopadhyay, M. J. Gutmann, M. Jimenez-Ruiz, D. B. Jochym, K. T.	(in preparation, 2015).

	Acid from Neutron Scattering and First-principles Density Functional Theory	Wikfeldt, K. Refson, and F. Fernandez-Alonso	
30	Ab-initio simulations and quasielastic neutron scattering measurements on single ion motions in molten NaF	F. Demmel and S. Mukhopadhyay	J. Chem. Phys., submitted (2015).

6.2 Presentations

	Conference	Title	Presenter
1	ECNS-2015 Zaragoza, Spain	Applications of neutron scattering to catalysts and energy materials	S.F.Parker
2	Laser Plasma Accelerator Workshop 2015, Guadeloupe, France	Plasma Wakefield Diagnostic Using Photon Acceleration	M. F. Kasim, P. N. Burrows, P. A. Norreys,
3	EJB Symposium, Amsterdam, NL	The influence of solvation on the catalytic properties of Fe(IV)oxo compounds	L. Bernasconi
4	Metals, Water and Sun 2015, Almeria, Spain	Photocatalysis in solution	L. Bernasconi
5	UK Neutron and Muon User Meeting, Leicestershire, UK	Ab initio modelling of catalytic processes in solution	L. Bernasconi
6	Advances in Modern Magnetic Materials, DLS	2D Cs-vacancy superstructure in iron-based superconductor Cs0.8Fe1.6Se2	D.G. Porter
7	Symposium on Energy Challenges & Mechanics, Aberdeen	Superstructures in Iron-Based Superconductors	D.G. Porter
8	ECNS-2015 Zaragoza, Spain	Poster: Monte Carlo simulations using McStas suite: "*Monte Carlo modeling of TOSCA neutron spectrometer: capability benchmarking and design of the beamline upgrade*	R. S. Pinna, G. Gorini, S. Rudic, F. Fernandez-Alonso
9	13th International Conference on Muon Spin Rotation, Relaxation and Resonance	DFT and μSR: towards a new symbiosis	P. Bonfa'

	(μSR2014), Grindelwald, Switzerland		
10	4th Italian Conference on Magnetism, Bologna, Italy	First principles analysis of magnetic and elastic properties of hexagonal perovskite-type $LaCrGe_3$	P. Bonfa'
11	Institute of Physics, Plasma Physics Conference, Milton Keynes	A convergent fast electron beam for laser-fusion applications	R. Scott
12	12th International Conference on Materials Chemistry (MC12), York	How terahertz vibrations can reveal pore breathing and structural instability in metal-organic frameworks	M. R. Ryder
13	British Zeolite Association Annual Meeting, Chester		M. R. Ryder
14	Workshop on Flexibility and Disorder in Metal–Organic Frameworks, Paris France		M. R. Ryder
15	Advanced Research Computing: High Performance Computing Showcase "Inspiring Bigger Questions, Inspiring the Next Generation,Oxford		M. R. Ryder
16	Molecular Spectroscopy Science Meeting (MSSM) 2015, Abingdon		M. R. Ryder
17	Oxford Solid Mechanics (OSM) Meeting, Oxford		M. R. Ryder
18	Solid Mechanics Seminar Series, Oxford		M. R. Ryder
19	Molecular Spectroscopy User Meeting, Abingdon	Poster: Mass-selective neutron spectroscopy beyond proton	M. Krzystyniak and F. Fernandez-Alonso
20	4th International Symposium on Energy Challenges and Mechanics - working on small scales, Aberdeen	Mass-selective neutron spectroscopy	M. Krzystyniak
21	ECNS-2015 Zaragoza, Spain	Poster: Mass-selective neutron spectroscopy	M. Krzystyniak, G. Romanelli, and F. Fernandez-

			Alonso
22	14th AeroCom meeting, Frascati, Italy	new Assessment of Aerosol-Cloud Interactions wirh ORAC (A)ATSR	M. Christensen
23	Faraday Discussions, Bangalore, India		S. Mukhopadhyay, M. J. Gutmann, and F. Fernandez-Alonso
24	Psi-k Conference, San Sebastian, Spain		S. Mukhopadhyay, M. J. Gutmann, and F. Fernandez-Alonso

7 APPENDIX: SCARF QUEUE USAGE 2014-15

7.1 General SCARF Queue

Open to all SCARF Users

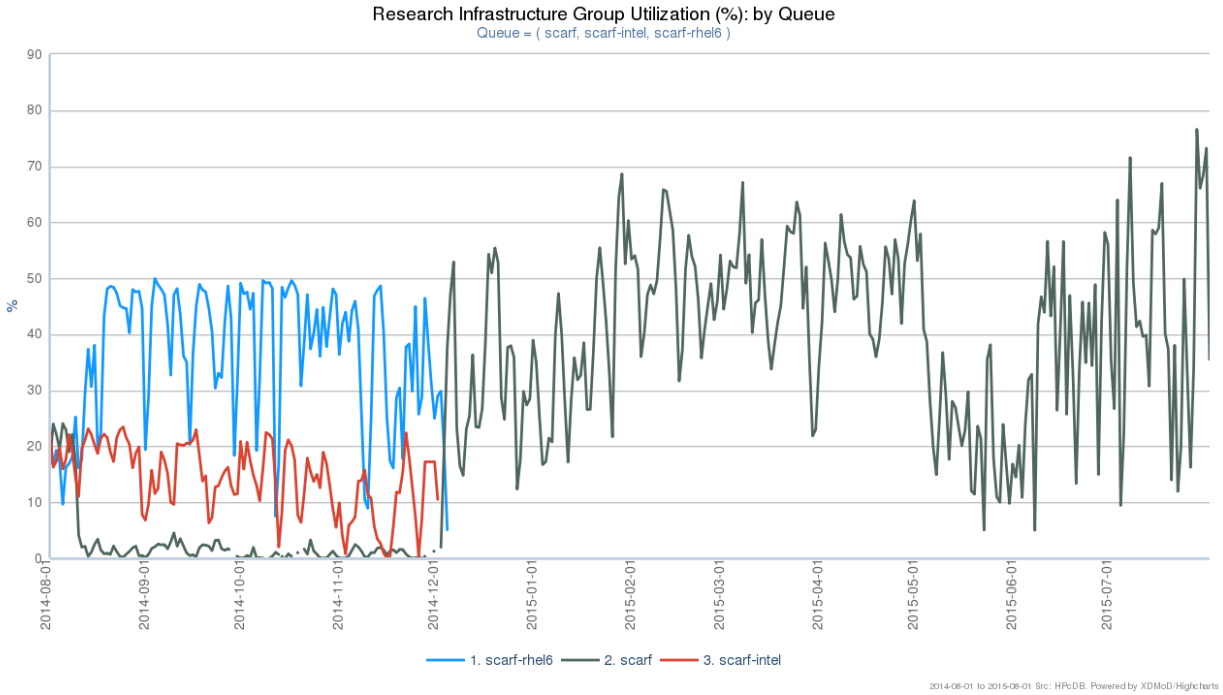

Figure 7.1.1: SCARF Queue Usage

In December, the migration to RHEL 6 was complete and the scarf-rhel6 queue used during the migration was closed. In addition the scarf-intel queue was closed as there was no longer any non-Intel equipment on SCARF, so there was no longer any difference between the scarf and scarf-intel queues.

We continue to use the mechanism inside LSF to allow groups of users to get preferential access to portions of hardware they have contributed money to purchase, while still making the hardware available to other users' jobs up to 24 hours in length. This is currently in place for ISIS on SCARF13 and ISIS and CLF FBI on SCARF14 and SCARF15

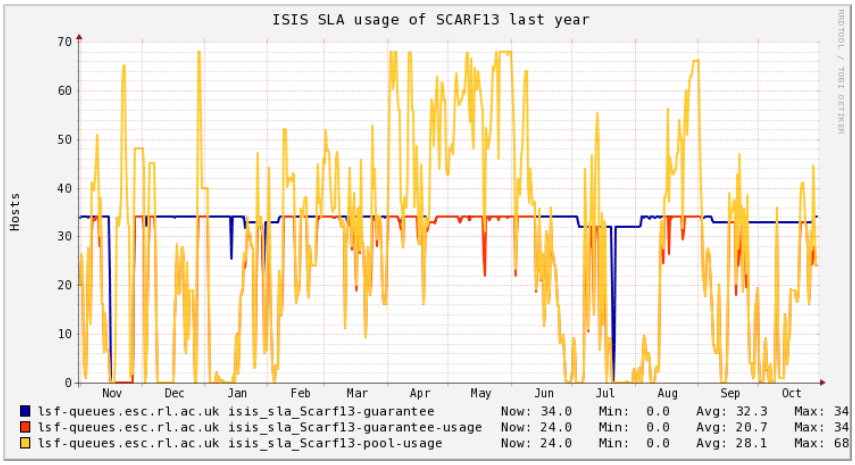

Figure 7.1.2: ISIS SLA Usage of SCARF 13

The blue line shows the level that is guaranteed to ISIS on SCARF13. The red line shows ISIS usage of their guarantee. The yellow line shows all ISIS usage. While usage varies over the year the average for the yellow line is close to the guaranteed figure, showing that on average ISIS are making use of the hosts they get priority access to.

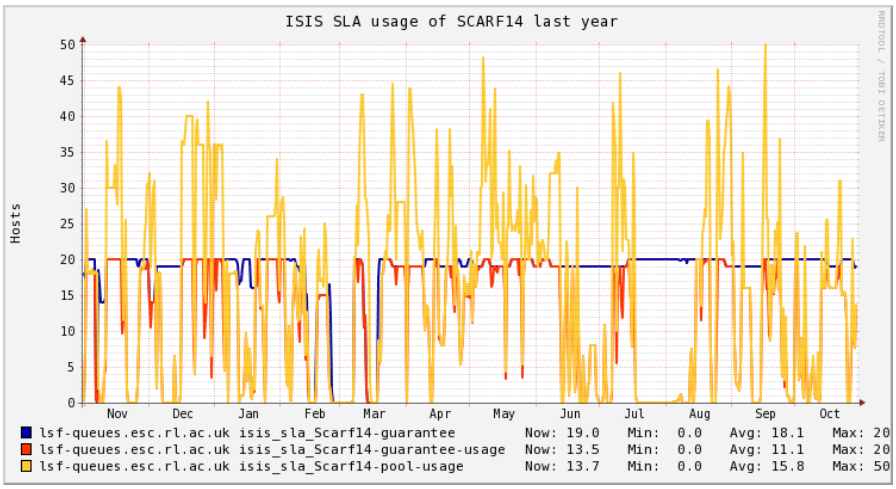

Figure 7.1.3: ISIS SLA Usage of SCARF 14

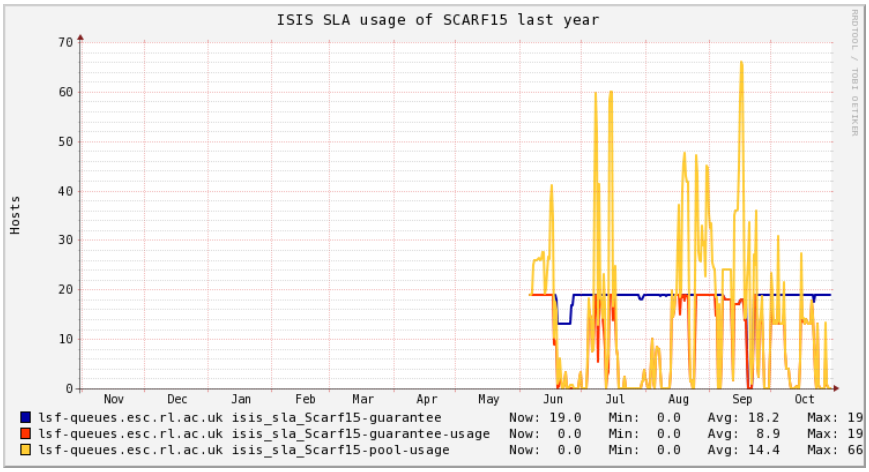

Figure 7.1.4: ISIS SLA Usage of SCARF 15

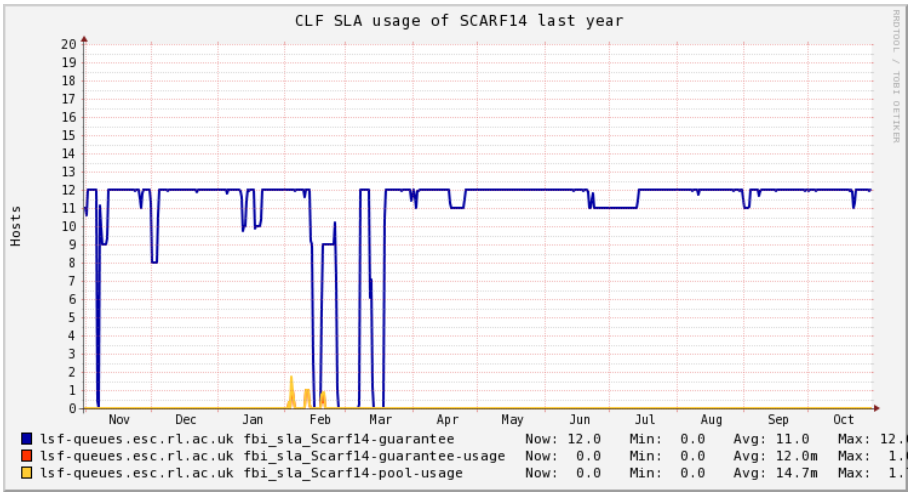

Figure 7.1.5: CLF SLA Usage of SCARF 14

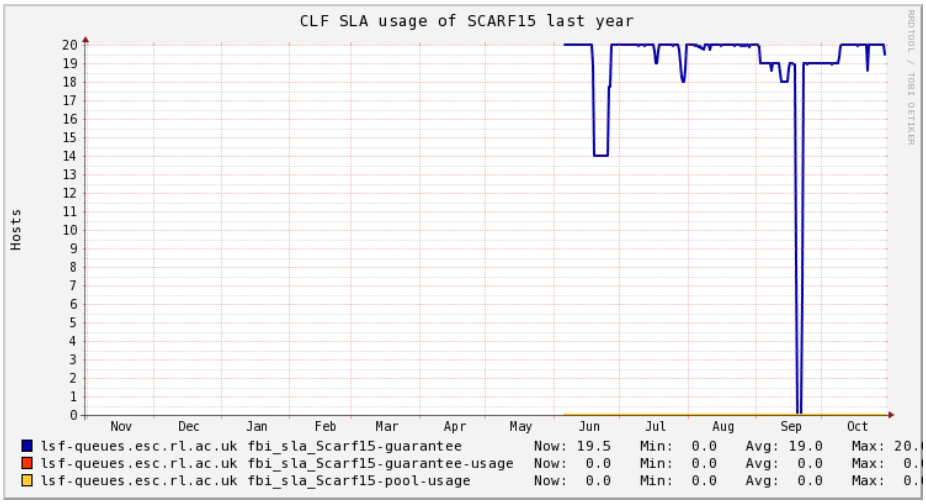

Figure 7.1.6: CLF SLA Usage of SCARF 15

The SCARF14 and SCARF15 plots for CLF FBI show that they have not yet begun making extensive use of their guaranteed resources

7.2 SCARF-Lexicon1 and Lexicon2 Queues

These queues are primarily for CLF use with a capacity of 256 and 544 CPU cores for SCARF Lexicon 1 & 2 respectively. The original Lexicon 1 nodes were replaced with 256 new cores in June 2013.

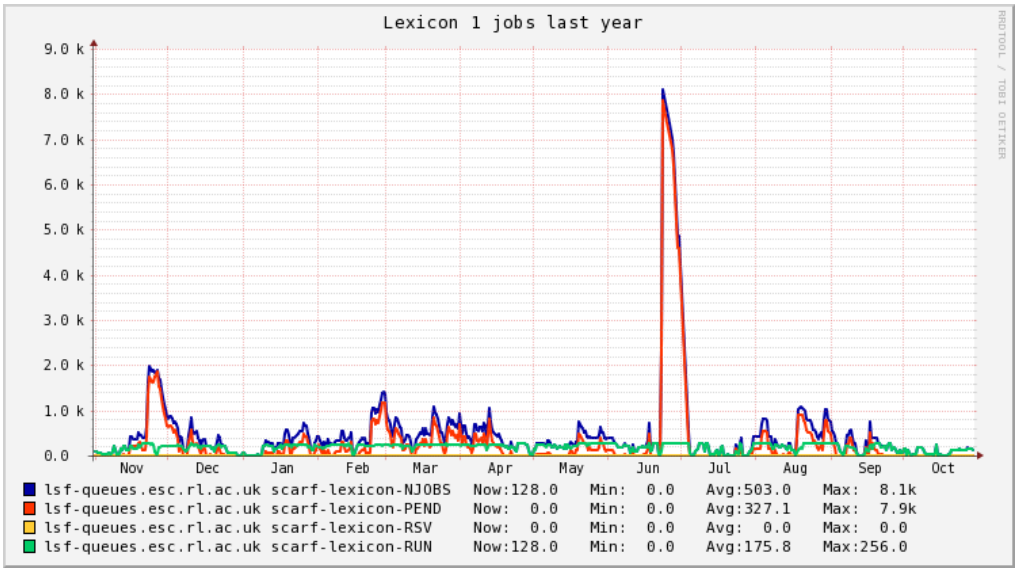

Figure 7.2.1: SCARF-Lexicon Usage

The graph for the SCARF-LEXICON queue shows significant usage, as it is available to CLF collaborators.

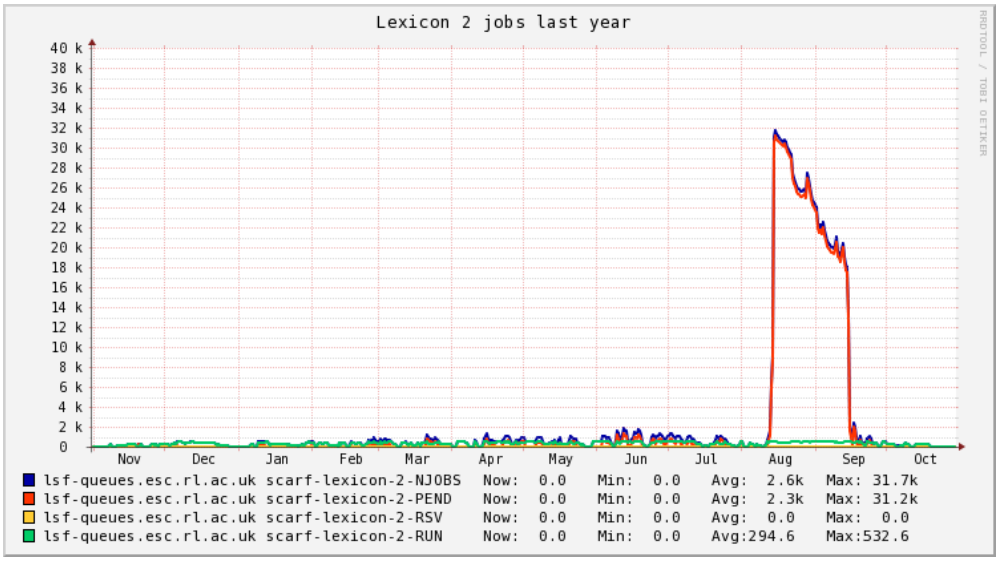

Figure 7.2.2: : SCARF Lexicon-2 Usage

SCARF-LEXICON-2 continues to be used for higher priority Lexicon users and on demand to support CLF experiments.

7.3 SCARF-IBIS

SCARF-IBIS has a capacity of 144 CPU cores.

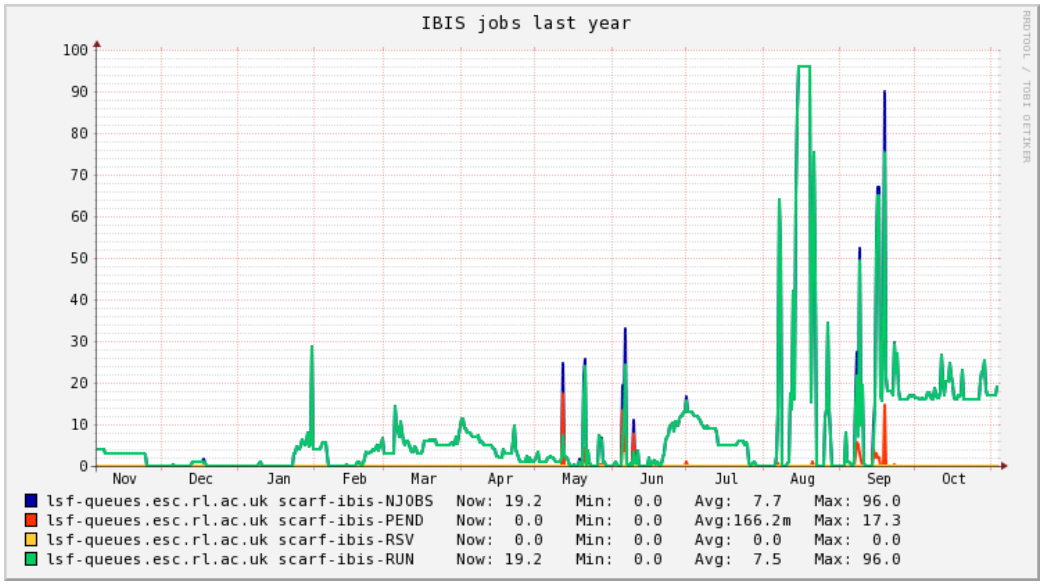

Figure 7.3.1: SCARF-IBIS Usage

7.4 SCARF Total Power draw (amps)

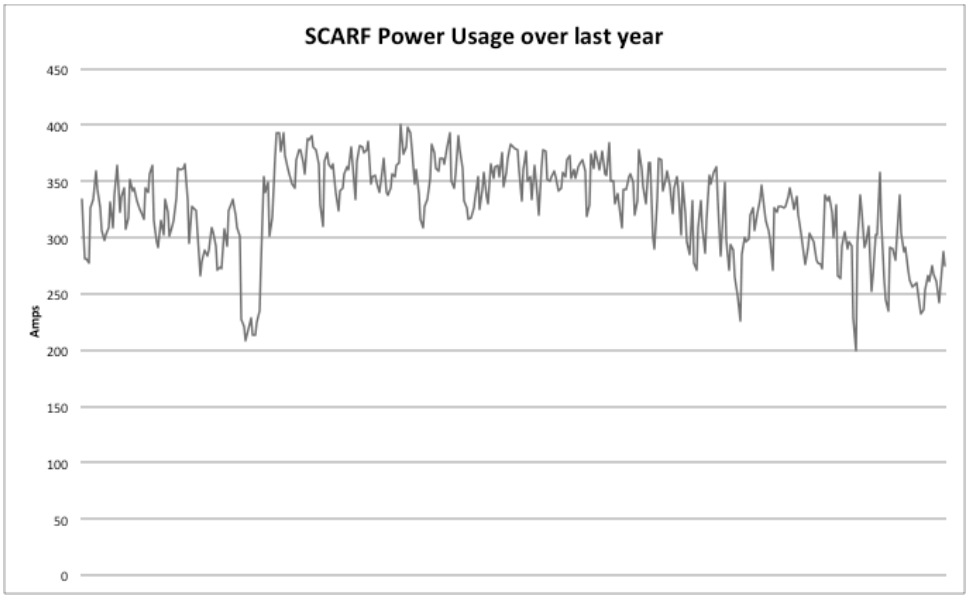

Figure 7.4.1: SCARF Power Usage

The approximate average power draw of the SCARF cluster (including Lexicon) is about 300 amps or 72 kW. This excludes the power needed to cool, pump and move cold air. The efficiency of SCARF in terms in Gflops/W is giving in the table below.

Year Purchased	Gflops/W
2010	0.32
2011	0.48
2012	0.50
2013	0.59
2014	0.98
2015	1.95

Figure 7.4.2: GFlops/W for SCARF generations of equipment

From the above table it is clear that the Gflops/W achieved increase per generation of the SCARF equipment. This supports the continual refresh rate of SCARF hardware rather than a big bang approach.

7.5 Filesystem Usage

The plot below outlines the use of the Panasas filespace on the SCARF service. The filespace is shared across a number of projects therefore not all space is available to SCARF users, but SCARF users benefit as increasing the amount of space also increases the bandwith to the storage as files are redistributed around the Panasas system automatically.

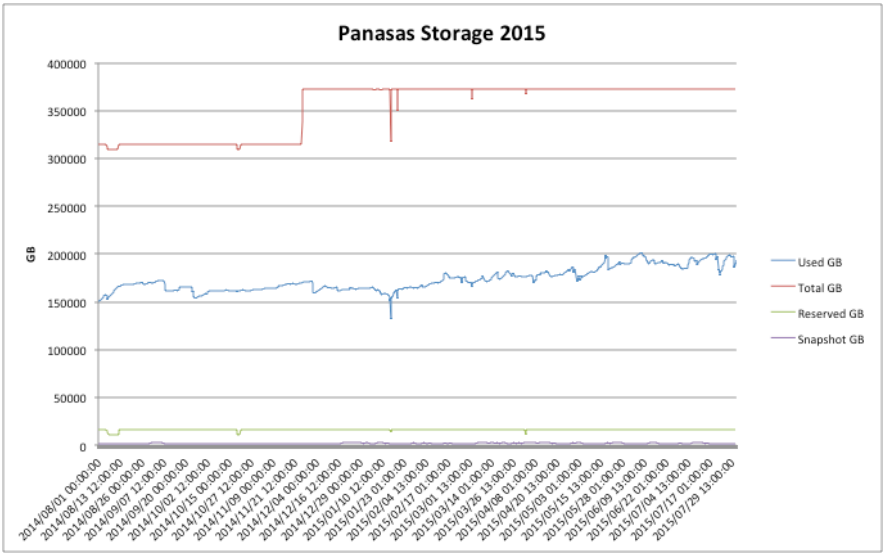

Figure 7.5.1: Filespace usage on the Panasas Storage

7.6 Networking

The diagram below shows the SCARF compute clusters embedded in the larger Research Infrastructure group's networking infrastructure. A change that has been taking place gradually has been the migration of SCARF equipment one step away from the core RIG network infrastructure to the switch labelled "HPC switch" in the diagram. This was necessary as the latest SCARF hardware now has faster host connections – up from 1 gigabit to 10 gigabit, which means that a faster uplink

is required to cope with the greater bandwidth demands from that equipment. As the faster host connections will become the new default, additional network capacity was required.

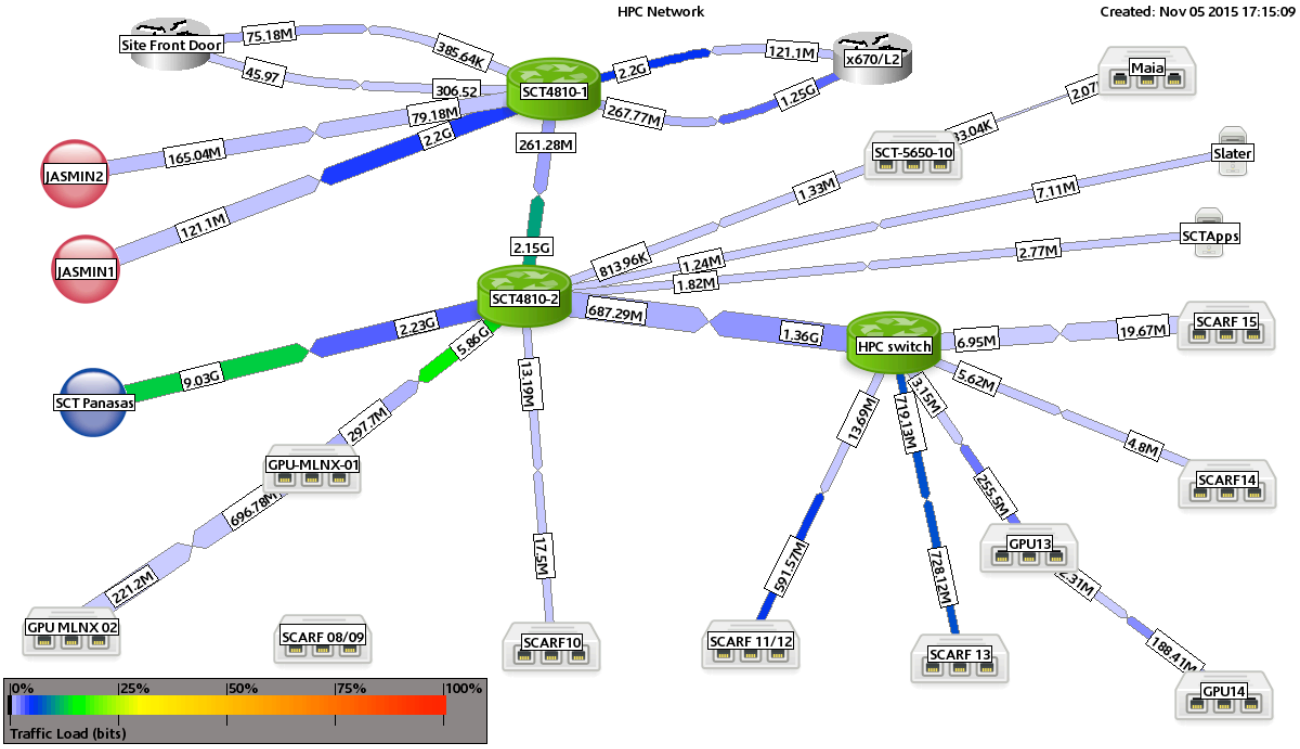

Figure 7.6.1: SCARF Network Topology

The following graphs outline the network traffic from the clusters. This captures traffic to the Panasas filesystems, backups and external traffic.

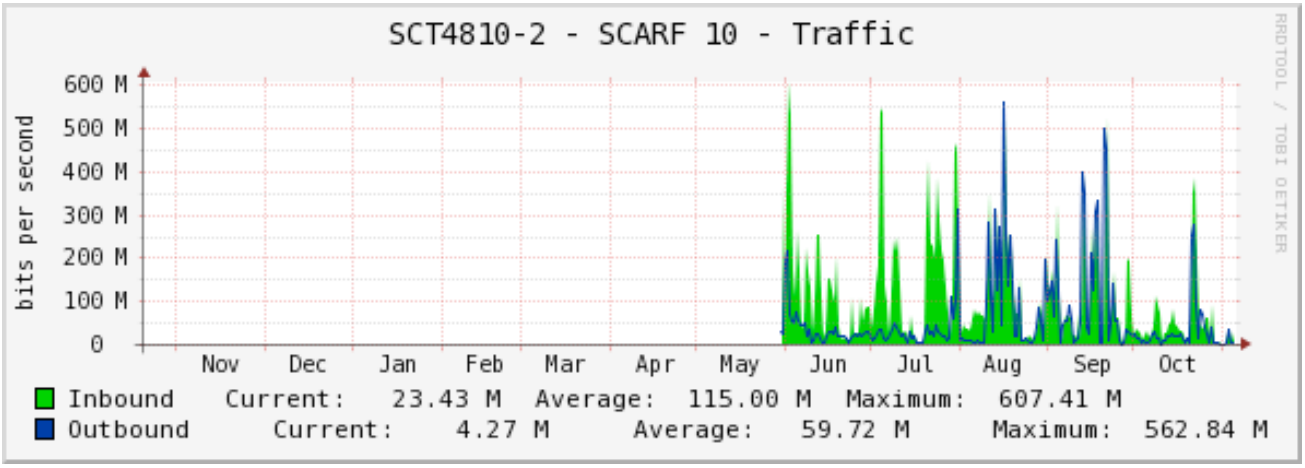

Figure 7.6.2: SCARF10 and Lexicon 2 Network Traffic

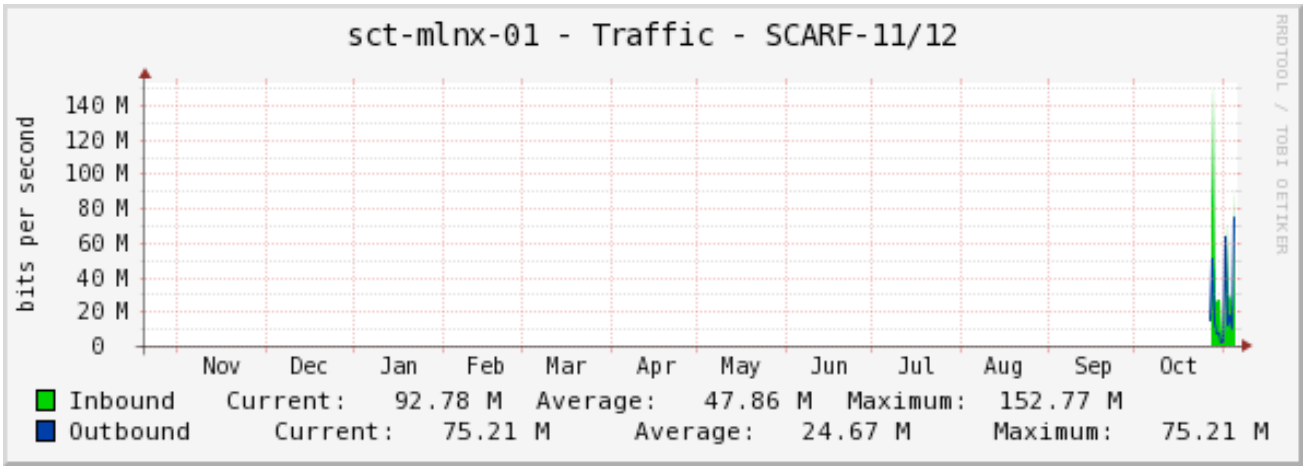

Figure 7.6.3: SCARF11 and SCARF12 Network Traffic

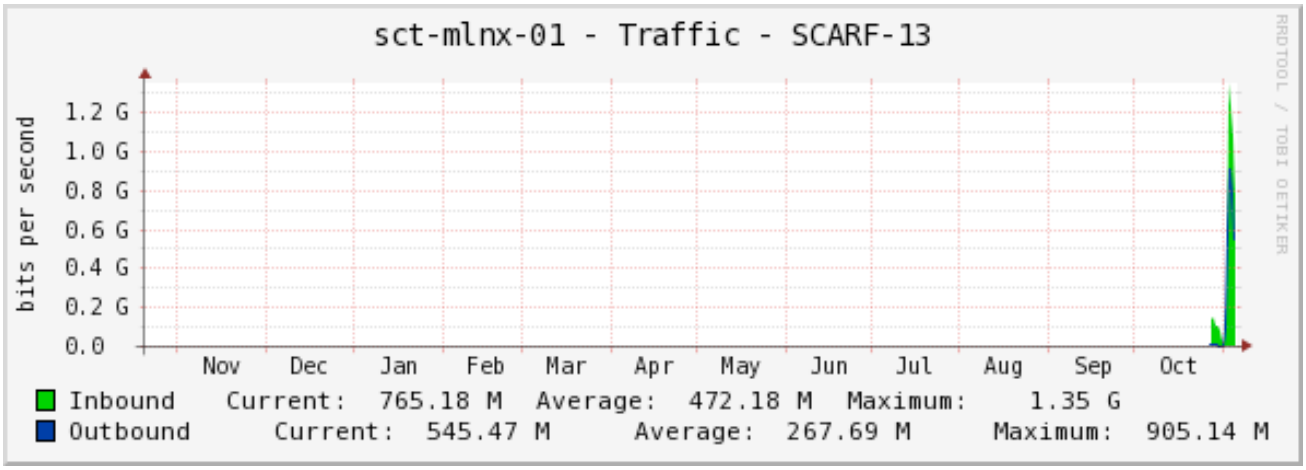

Figure 7.6.4: SCARF13 and Lexicon 1 Network Traffic

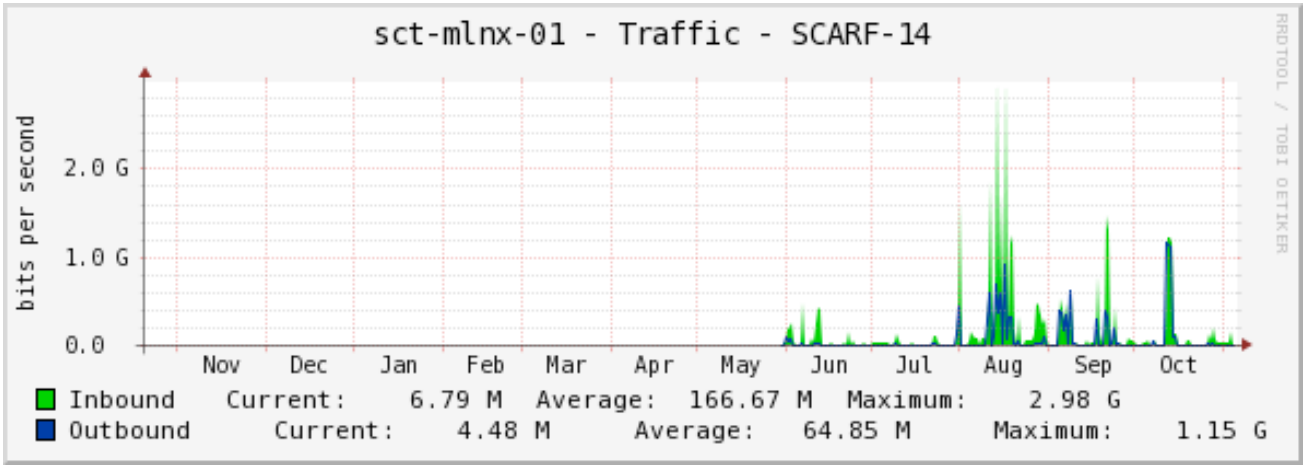

Figure 7.6.5: SCARF14 Network Traffic

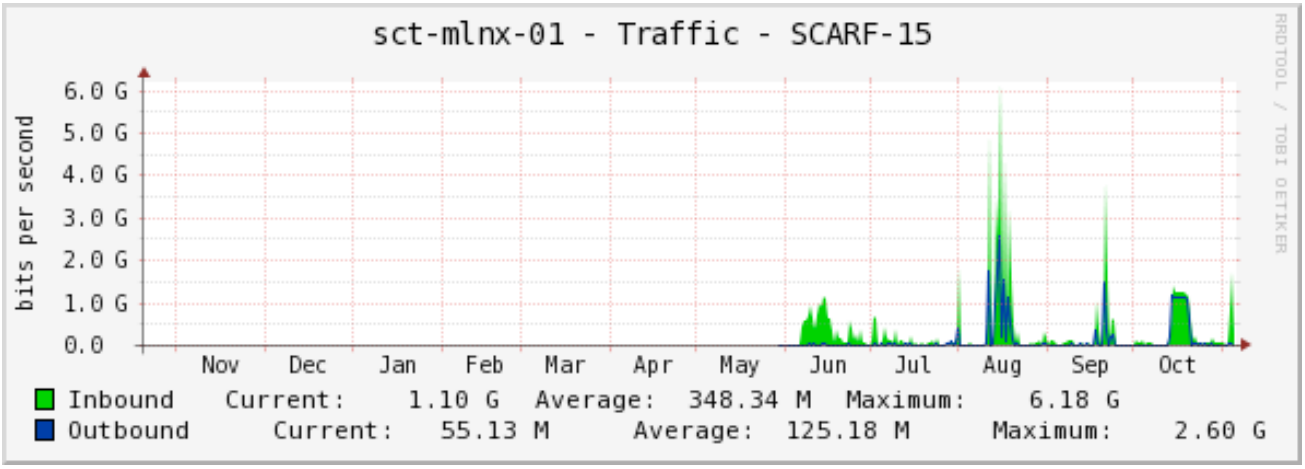

Figure 7.6.6: SCARF15 Network Traffic

8 APPENDIX: SCARF DEVELOPMENTS

It has been a busy year for the SCARF service. Users' will have noticed most impact with the additional of capacity and upgrades to applications. However, a lot of effort goes into improving the management of SCARF.

8.1 Technical Developments

- In June the 2015 hardware tranche of dual Intel E5-2650v3, providing 1360 cores was made available.
- 30TB of storage space was added to SCARF's storage backend in December 2014
- Migrations of the SCARF hosts to a new network topology took place over the year
- The migration to RHEL 6 was completed in December 2014.
- SCARF08 and SCARF09 were removed from service
- Access to SCARF is now available using ssh keys improving access for non-STFC users
- A new website for SCARF documentation was released in September 2014
- A new website for examining SCARF usage was released in June 2015

8.2 Application Stack

A selection of new or updated applications is in the table below:

Application	Area	Version
CASTEP	Computational Chemistry	8.0
AMBER	Computational Chemistry	14.10
netCDF	data model, library, and file format for storing and managing data	4.3.2
DL_POLY	DL_POLY is a general purpose classical molecular dynamics (MD) simulation software	4.07
Intel compiler	Fortran, C, C++ compilers and Maths libraries	15.3
PGI compilers	Fortran, C, C++ compilers and Maths libraries	15.3

Figure 8.2.1: SCARF Application Stack

A full list of the available software on SCARF can be found on the SCARF website:
http://www.scarf.rl.ac.uk/applications-libraries